



university of
 groningen

faculty of mathematics
 and natural sciences



Fluid-structure interactions of spheres in pipelines, using computational and port-Hamiltonian approaches

Bachelor Project: Mathematics and Applied Mathematics

August 15, 2016

Student: Joseph D. Field

Daily Supervisor: Henk Seubers, MSc

First Supervisor: Prof. dr. A.E.P. Veldman

Second Supervisor: Prof. dr. A.J. van der Schaft

INCAS³ Supervisor: Peter van Hengel

Abstract

Initially, this thesis looks at computational simulations of spherical sensors, or *motes*, travelling through fluid-filled pipelines with no free surface. Two factors are important in this part of the study: to understand whether qualitative flow behaviour can be gained from simple numerical simulations, and to analyse the efficiency of a *quasi-simultaneous* iterative coupling method, compared to standard coupling methods. Regarding flow behaviour, simulation results find that motes tend to converge towards the centre of the pipe, regardless of their initial release point, but that there may be a *region* of equilibrium around the pipe's central axis. Simulation data also finds that the quasi-simultaneous method is much more efficient than standard methods, especially when simulating the behaviour of neutrally dense motes. The second part of the study then attempts to describe the fluid-structure interaction in the framework of port-Hamiltonian systems, using a combination of *mechanical* and *hydraulic* domains. Different approaches are attempted here, resulting in coupling equations built on an assumed Hamiltonian form. Finally, a bridge between the two parts of the thesis is attempted, describing the numerical coupling scheme using port-Hamiltonian language.

Contents

1	Introduction	4
2	Literature Review	5
3	Mathematical Model	6
3.1	The equations for fluid flow	6
3.2	Geometric description of the problem	6
3.3	Derivation of added mass	8
4	Numerical Simulation	11
4.1	Coupling constraints	11
4.2	Numerical methods	12
5	Computational Results	14
5.1	Discretization of the geometry	14
5.2	Results	14
5.2.1	Initial vertical position	14
5.2.2	Increasing mote radius	18
5.2.3	Initial horizontal position	21
5.3	Summary of numerical simulations	23
6	Port-Hamiltonian Systems	25
6.1	Prerequisites	25
6.1.1	Hamiltonian mechanics	25
6.1.2	Port-Hamiltonian definitions	26
6.1.3	An intuitive example: the mass-spring system	28
6.2	Description of the model	29
6.2.1	Governing equations	30
6.2.2	Attempting to couple the equations	32
6.2.3	A different coupling perspective	34
7	A Numerical Port-Hamiltonian Scheme	37
7.1	Description of the numerical model	37
7.2	Introducing an iterative scheme	39
8	Discussion	46
8.1	Possible extensions	46
9	Appendices	48
9.1	Table of geometric models	48
9.2	Additional results	48
9.3	Table of domain classifications	49
9.4	Canonical Hamiltonian form	50
9.5	Non-symmetric computations	52
9.6	Co-simulation: an alternate approach	53

1 Introduction

Understanding the motion and behaviour of fluids is a popular area of research, not only in academia but also in countless areas of industry. Over the past decades, the growth of Computational Fluid Dynamics (CFD) as a tool for investigation and verification has cemented its place as a bridge between theory and experiment. It is therefore understandable that many companies wish to incorporate CFD analyses into projects which include fluids, to either confirm experimental data, or even to create an initial model on which to base future experimentation.

This project revolves around a problem brought to Prof. A.E.P. Veldman by INCAS³, a research institute based in Assen. INCAS³ has been developing a remote sensor system, WisemotesTM (referred to as *motes* throughout this thesis), designed to perform flow measurements in inaccessible areas, such as pipelines. This is an important tool for a large number of industries, as pipelines are often not directly measurable, yet they contain a huge amount of information regarding the flow behaviour, obstructions, or even possible leaks. In light of this, the general question that INCAS³ want to investigate is: *Can the motion of a remote spherical sensor travelling through a pipeline be modelled accurately by existing CFD software?*

A question such as this obviously has a variety of facets: *What is the fluid being modelled? What is the geometry of the pipeline that will be simulated? What are the attributes of the sensors?* For this reason, it was best to look at simple, qualitative cases to determine any fundamental flow behaviour, and to get an immediate understanding of the problem in its most basic sense.

A particular focus of INCAS³'s question was to determine the effects of two different parameters; the first to be looked at was the effect of the initial release position of the mote, and what impact it had on the resulting trajectories. To follow, we then looked at the geometry of the mote, asking what impact the mote has on the fluid when its radius is increased, relative to the radius of the pipe. Other areas of investigation were suggested by INCAS³, such as the varying of the mote mass, or examining the effect of gravity in inclined pipes, but for the scope of this thesis it was best to focus on just the two chosen areas. The mathematical model of the problem is explained in Section 3.

This study then looks at the numerical modelling and simulation of fluid-structure interactions (FSI) in a simple pipeline geometry. In this section, there are then two further areas of focus: the qualitative behaviour of simple, coarse-grid flow simulations; and the efficiency of a *quasi-simultaneous* iterative method over standard coupling methods. The quasi-simultaneous method used here is a *coupled* iterative process between a fluid and a solid body, such that information is shared between components at each time-step, rather than a traditional 'cause-and-effect' iterative method. This means that the fluid 'anticipates' the movement of the solid body at each step, reducing the total computational effort. All of these topics are treated in more detail in Section 4, with numerical and experimental results being discussed further in Section 5.

The second approach of this thesis is to look at FSI models in terms of a *port-Hamiltonian* framework. To put (almost too) simply, port-Hamiltonian systems can be used to describe systems with multiple components, or multiple physical domains, using energy as the 'currency' transferred between each part. With this idea, an attempt has been made to describe the FSI system in terms of *mechanical* and *hydraulic* domains, governed by the idealised transfer of energy. This topic is investigated in Section 6. To end the thesis, in Section 7 attempts are made to describe the numerical model using port-Hamiltonian language, to form a bridge between the two disciplines.

2 Literature Review

The study of complex fluid flow is such a diverse area of research that it can be approached from a number of different directions. From a computational standpoint, an exposition by Anderson [1] gives a general overview of the subject of computational fluid dynamics, aiming to be a *pre-graduate* level textbook on CFD. This text covers a large amount of preparatory material, starting with the derivations of the general fluid equations, extending into a study of the numerical techniques used in CFD models, culminating in a review of possible applications.

At a more specific level, work by Veldman et al. [35, 36] gives a deeper analysis of the accuracy of fluid-structure interaction models, with a focus on the robustness of fluid-solid coupling techniques. This work will be drawn from in Sections 3 and 4, where we analyse the numerical approach for modelling a solid body in a fluid domain. Veldman et al. also make note of the impact of *added mass* within a modelling framework, which is explored more generally by Brennen [4], Fackrell [8], and Pantaleone and Messer [18]. In a similar investigation to this one, focusing on the effect of added mass on computational models, Causin et al. [5] investigate the numerical instabilities of potential flows inside linear elastic thin tubes.

The understanding of solid/particle behaviour in fluids has also been looked at in some detail, with pioneering experimentation being done by Segré and Silberberg [24, 25], whereby an asymmetric radial equilibrium distance was observed for particles travelling in slow fluid flow. Adding to this, works by Cox and Brenner [6], Hogg [10], Schonberg and Hinch [23], and Yang et al. [38, 39] further investigate the migration behaviour of spheres and spherical particles in different flow patterns. More recently, a study by Liang [14] focuses on the numerical investigation of more general geometries in pipe flow, namely industrial ‘pigs’, or *Pipeline Inspection Gauges*. Although almost all of these works are beyond the level of this thesis, they provide an interesting baseline for what could be expected from the computational models.

An introduction to port-based modelling is given by Paynter [19], while for an introductory summary of port-Hamiltonian systems, works by van der Schaft [29], van der Schaft and Jeltsema [31] and van der Schaft and Cervera [30] offer a good foundation. Interdisciplinary articles useful to this study can be found by Talasila et al. [26], who give a *discrete* port-Hamiltonian formulation, and Lequeurre and Tucsnak [13], who presents a well-posed port-Hamiltonian formulation of two simple, one-dimensional FSI systems.

Finally, works by Morrison [16, 17] give rigorous overviews of Hamiltonian fluid dynamics, albeit again in language far higher than a Bachelor’s thesis. Articles by Wirosuetiso [37], Antoniou and Pronko [2] and van Saarloos et al. [32] offer similar descriptions, while Salmon [22] presents a more general review of concepts in this field.

3 Mathematical Model

In this section we outline the necessary physical equations that will be important to the study, and a geometric description of the problem is shown, to give a foundation for the numerical simulations. To end the section, the concept of *added mass* is explained in detail, describing the additional force felt by a solid in non-steady flow.

3.1 The equations for fluid flow

The two fluid equations used here in this thesis are governed by the conservation of mass, and the conservation of momentum, with respect to an *incompressible* fluid, i.e., a fluid which has constant density. Here, the assumption of incompressibility is a valid one, as this project has a focus only on one-phase, liquid flows, such as water or oil. These equations form the *incompressible Navier-Stokes equations* [1]

$$\frac{\partial \mathbf{u}}{\partial t} + (\mathbf{u} \cdot \nabla) \mathbf{u} = -\frac{1}{\rho} \nabla p + \nu \nabla^2 \mathbf{u}, \quad (1)$$

$$\nabla \cdot \mathbf{u} = 0, \quad (2)$$

where \mathbf{u} is the flow velocity, ρ is the fluid density, p is the fluid pressure, and ν is the kinematic viscosity.

Note that on its own, Eq. (1) is a system of three equations in four unknowns; the three velocity components, $\mathbf{u} = (u, v, w)^T$, and the pressure term, p . Therefore, with the inclusion of the incompressibility condition (2), the system is then closed, and solutions can be found. That said, no general solution to these equations is known, so they must be solved using additional simplifications, or alternatively they can be tackled numerically.

A secondary form of the Navier-Stokes equations is sometimes used [35], taking the operator form

$$\mathcal{M} \mathbf{u} = 0, \quad \frac{\partial \mathbf{u}}{\partial t} + \mathcal{C}(\mathbf{u}) \mathbf{u} = -\mathcal{G} p + \mathcal{V} \mathbf{u}. \quad (3)$$

In this form, \mathcal{M} represents the divergence operator, $\mathcal{C}(\mathbf{u}) \mathbf{u} \equiv (\mathbf{u} \cdot \nabla) \mathbf{u}$ is the convection operator, \mathcal{G} denotes the pressure gradient, and $\mathcal{V}(\mathbf{u}) \equiv \nu \nabla^2$ is the diffusion operator. This construction is used by Veldman et al. [35, 36] to describe the discretization of the Navier-Stokes equations, but this will not be covered in this thesis, as we do not wish to explore the specific integration methods used in the computational models.

3.2 Geometric description of the problem

Given that this project looks primarily at qualitative behaviour, the simplest geometry to investigate is a uniform length of pipe, with a uniformly dense, spherical mote inside, shown by Fig. 1.

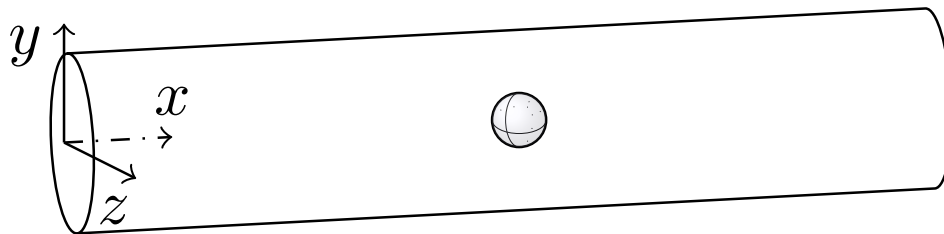


Figure 1: 3D representation of a mote in a simple pipeline geometry.

Figs. 2 and 3 show a more detailed cross-section of the pipe geometry, assuming the flow inside the pipe is governed by a three-dimensional Poiseuille velocity profile. Here we look at a pipe section of length L , and radius R , in which a spherical mote of radius r travels. We assume there to be a defined inlet flow, which we take to be a fully-developed Poiseuille flow profile, i.e., we model the section of the pipe *after* the hydrodynamic entrance region. The outlet condition will be taken to be a zero pressure condition, rather than taking an outlet velocity condition¹. The assumption of using a Poiseuille flow to model the pipelines is validated by the fact that this study focuses exclusively on laminar flow, ignoring the occurrence of turbulence.

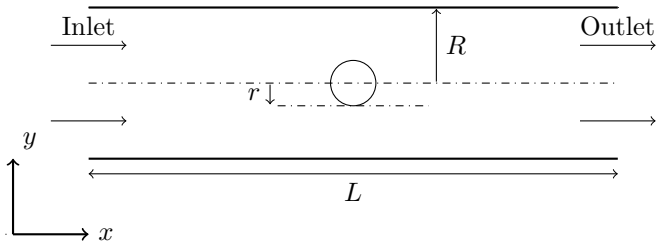


Figure 2: Lengthwise cross-section of the 3D geometry.

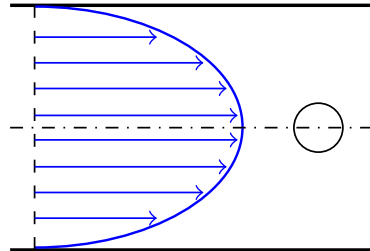


Figure 3: Lengthwise cross-section of 3D Poiseuille flow.

To add to the governing fluid equations, we must also apply some additional constraints on the model, to make it agree more closely with physical expectations. Firstly, we require that there is no mass flux through the pipe wall, and also assume there to be a no-slip condition where the pipe meets the fluid. This mirrors real fluid behaviour, and is akin to stating $\mathbf{u}_{\mathcal{P}} = \mathbf{0}$, where the subscript \mathcal{P} denotes all points at the interface of the pipe and the fluid.

Secondly, we expect the fluid and the mote to share physical characteristics along their shared boundary surface. Therefore we impose the *kinematic* condition that fluid particles have the same velocity and acceleration as the part of the mote that they are touching;

$$\begin{aligned}\mathbf{u}_s &= \mathbf{u}_f =: \mathbf{u}_{\Gamma}, \\ \dot{\mathbf{u}}_s &= \dot{\mathbf{u}}_f =: \dot{\mathbf{u}}_{\Gamma},\end{aligned}\tag{4}$$

where the subscript Γ denotes all points at the interface of the fluid and the mote².

Similarly, we employ a *dynamic* condition requiring that the fluid force acting on the mote is equal in magnitude, but negative, to the force that the mote exerts on the fluid, which we denote by

$$\mathbf{f}_{s \rightarrow f} = -\mathbf{f}_{f \rightarrow s}.\tag{5}$$

Finally, to make the problem analytically simpler, we assume that the flow can be modelled by way of a *potential flow*, i.e., there exists a scalar *potential function*, ϕ , such that the flow velocity vector is determined by

$$\mathbf{u} = \nabla \phi.\tag{6}$$

This assumption is primarily used to simplify the derivation of the *added mass* in Section 3.3, whereas in the computational model the Navier-Stokes equations are solved numerically, so there is no need for such a simplification.

¹This condition was used as it made the computational models slightly more stable.

²For the first part of this thesis, we will use the subscripts s and f to denote *solid* and *fluid* respectively. We also use the terms *solid*, *mote*, and *body* interchangeably.

3.3 Derivation of added mass

Before looking at the numerical simulations of the problem, the concept of *added mass* must be explained, both to understand the difficulties that exist in analysing the physical flow behaviour [4, 8], and also to understand the computational inefficiency of certain iterative methods [35, 36]. The most basic explanation of *added mass* is that it represents the additional force needed to accelerate a body in a fluid, compared to the force needed to accelerate in a vacuum.

Let us imagine a solid body in a fluid, such that the body is moving rectilinearly at a constant rate, and the fluid is otherwise at rest over a domain Ω . The body has a kinetic energy

$$T_s = \frac{1}{2}m|\mathbf{v}|^2, \quad (7)$$

where \mathbf{v} is the velocity of the body, and m is the body mass. Similarly, the fluid has a kinetic energy

$$T_f = \int_{\Omega} \frac{\rho}{2} |\mathbf{u}|^2 d\Omega, \quad (8)$$

where ρ is the (constant) fluid density, and \mathbf{u} is the pointwise fluid velocity.

If we now consider that the body accelerates in the direction of motion, then its kinetic energy will increase, due to the increase in velocity. Similarly, due to the greater disturbance by the body, the kinetic energy of the fluid will also increase. However, this energy increase must be supplied from somewhere, so the body must do additional work on the fluid. This additional work is experienced by the body in the form of an extra drag force, \mathbf{F} . Thus, the extra drag comes from the acceleration of the body, $\mathbf{a} = d\mathbf{v}/dt$, such that

$$\mathbf{F} = -\tilde{m} \frac{d\mathbf{v}}{dt}. \quad (9)$$

It is therefore convenient to view the mass term \tilde{m} as the *added mass* of the fluid being accelerated by the body. What is important to understand is that there is no specific region of fluid which will be accelerating, but instead that each point in the domain Ω accelerates by some (possibly infinitesimal) degree, such that the total kinetic energy of the fluid increases accordingly.

With this in mind, we present here a derivation for the added mass of a sphere accelerating in an infinite domain of otherwise stationary fluid, such that the fluid velocity is always zero at the (unattainable) boundary³.

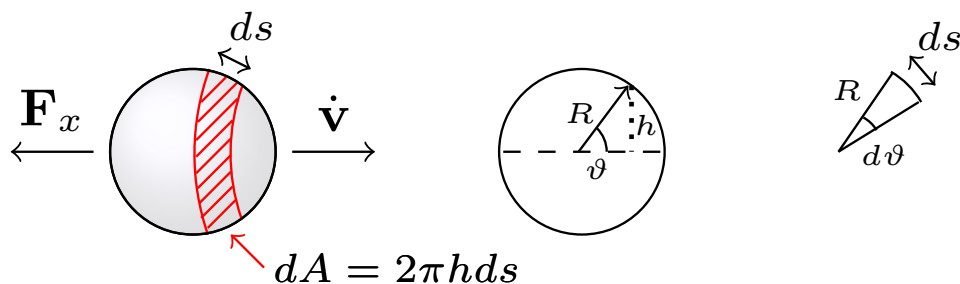


Figure 4: Calculating the added mass of a sphere accelerating in the x-direction, using the centre of the sphere as the coordinate origin.

³This derivation is an expansion of the class notes [7], but a more general explanation involving tensor notation can also be found in [27].

Without loss of generality, let us assume that the body accelerates in the x-direction, as seen in Fig. 4, with the coordinate origin imposed at the centre of the sphere. To make calculations simpler, we can instead use polar coordinates to then utilise the potential function

$$\phi(r, \vartheta) = v \frac{R^3}{2r^2} \cos \vartheta \quad (10)$$

to govern the behaviour of axisymmetric flow around a sphere. From Fig. 4, we use the infinitesimal approximations

$$ds = R d\vartheta, \quad dA = 2\pi h ds, \quad h = R \sin \vartheta, \quad ds_x = \cos \vartheta ds, \quad (11)$$

to find the *projected* area of the sphere

$$dA_x = \cos \vartheta dA. \quad (12)$$

Note that the reason we use the projected area is because we are looking for the horizontal force acting upon each point of the body surface, i.e., we integrate over the entire surface, denoted by Γ , such that

$$F_x = \int_{\Gamma} p dA_x. \quad (13)$$

Also, using the approximations (11), this integral can be written in the polar form⁴

$$F_x = \int_0^\pi 2\pi p R^2 \cos \vartheta \sin \vartheta d\vartheta. \quad (14)$$

With this in mind, we can use the reduced *Bernoulli equation for unsteady flow*

$$\rho \frac{\partial \phi}{\partial t} + \frac{1}{2} \rho |\nabla \phi|^2 + p = 0 \quad (15)$$

to then solve for the pressure, such that

$$p = -\rho \left(\frac{\partial \phi}{\partial t} + \frac{1}{2} |\nabla \phi|^2 \right). \quad (16)$$

Using the chosen potential function, we can calculate

$$\frac{\partial \phi}{\partial t} = \dot{v} \frac{R^3}{2r^2} \cos \vartheta, \quad (17)$$

$$\nabla \phi = \left[\frac{\partial \phi}{\partial r}, \frac{1}{r} \frac{\partial \phi}{\partial \vartheta} \right]^T = \left[-v \frac{R^3}{r^3} \cos \vartheta, -v \frac{R^3}{2r^3} \sin \vartheta \right]^T. \quad (18)$$

Substituting these terms into the force integral, at the radial distance $r = R$, we find

$$\begin{aligned} F_x &= \int_0^\pi -\rho \left(\frac{\partial \phi}{\partial t} + \frac{1}{2} |\nabla \phi|^2 \right) 2\pi R^2 \cos \vartheta \sin \vartheta d\vartheta, \\ &= - \int_0^\pi \rho \left(\dot{v} \frac{R}{2} \cos \vartheta + \frac{1}{2} \left[-v \cos \vartheta, -\frac{1}{2} v \sin \vartheta \right]^2 \right) 2\pi R^2 \cos \vartheta \sin \vartheta d\vartheta, \\ &= - \int_0^\pi \rho \left(\dot{v} \frac{R}{2} \cos \vartheta + \frac{1}{2} \left(v^2 \cos^2 \vartheta + \frac{1}{4} v^2 \sin^2 \vartheta \right) \right) 2\pi R^2 \cos \vartheta \sin \vartheta d\vartheta, \\ &= -\rho \dot{v} \pi R^3 \int_0^\pi \cos^2 \vartheta \sin \vartheta d\vartheta - \rho v^2 \pi R^2 \int_0^\pi \left(\sin \vartheta \cos^3 \vartheta + \frac{1}{4} \cos \vartheta \sin^3 \vartheta \right) d\vartheta. \end{aligned} \quad (19)$$

⁴Note that we implicitly assume that the pressure is only dependent on ϑ , i.e., we assume that the force will be symmetric over the solid body.

The second integral involves a function that is rotationally symmetric of order 2 around the point $(\pi/2, 0)$, and is therefore equal to zero. This finds that the force acting on the body is instead

$$F_x = -\rho\dot{v}\pi R^3 \int_0^\pi \cos^2 \vartheta \sin \vartheta \, d\vartheta. \quad (20)$$

Using the substitution $t = \cos \vartheta$, we find the result

$$\begin{aligned} F_x &= \rho\dot{v}\pi R^3 \int_1^{-1} t^2 \, dt \\ &= -\rho\dot{v}\pi R^3 \int_{-1}^1 t^2 \, dt \\ &= -\frac{2}{3}\rho\pi R^3 \dot{v}, \end{aligned} \quad (21)$$

where $\dot{v} = d\mathbf{v}/dt$ is the body acceleration. Therefore, using Newton's Second Law (9), it must be that the added mass is given as⁵,

$$m_{ad} := \tilde{m} = \frac{2}{3}\rho\pi R^3. \quad (22)$$

Although it is not immediately obvious, this result has two areas of importance. The first is a pre-emptive explanation about the effect of added mass, as the stability of standard iterative methods relies on the ratio

$$\frac{m_{ad}}{m_s} \quad (23)$$

being less than one. That is to say, to guarantee numerical convergence of the iterative coupling process, we need that the added mass of the fluid is not greater than the actual mass of the solid body. Within the idealised, infinite domain, this means that as long as the density of the solid is greater than half the fluid density, then this ratio condition will be satisfied.

However, in the physical model we are not looking at unbounded fluids in an infinite domain. When the mote travels through a pipeline, the flow is likely to be non-steady, meaning that there will be a succession of accelerations, and therefore a succession of added mass values. If the mote is relatively wide with respect to the pipe diameter, then it may be that the fluid being disturbed is unable to move around the mote, so the total added mass could become very high; indeed, if the radius of the mote is increased to *almost* the radius of the pipe, then it will essentially be acting on *all* of the downstream and upstream fluid, which more than likely has a greater total mass than the mote.

For this reason, the added mass ratio is an important metric for understanding the inefficiency of certain iterative methods, and will be explored in more detail in Section 5, with respect to increasing the size of the mote.

Secondly, in terms of the mote's behaviour within the pipe, the concept of added mass gives a way to understand the impact that the pipe walls have on the model, compared to the unbounded domain. As the mote travels through the pipe, it will disturb the surrounding fluid, which may not necessarily be able to redistribute itself smoothly within the pipe. This is likely to cause extra forces within the pipe, which will act on both the fluid *and* the mote. Thus, non-steady flows within a pipeline are not necessarily easy to understand, as just a simple parameter change may cause drastically different flow behaviour.

⁵It is important to understand that we would arrive at the same formula had we taken *any* arbitrary acceleration, however it is much easier to compute for a single direction.

4 Numerical Simulation

In this chapter, the computational experimentation will be explained, starting with an overview of the discretized model equations. After this, a brief comparison of the *quasi-simultaneous* method to ‘traditional’ iteration methods will be made. A more detailed account of discretization procedures, utilising more complex geometries, can be found in [5, 34, 35, 36].

4.1 Coupling constraints

When deciding to use numerical techniques to solve coupled equations, there are two possible routes that can be taken; a *monolithic* approach combines the coupled equations into a single set of equations which are then solved simultaneously, while a *partitioned*, or *segregated*, approach opts to keep the equations as two separate systems, governed by a relationship of shared information. The monolithic method is more robust, as the solutions are found as a whole, but this is not necessarily an easy task, especially for complicated systems involving different physical domains. The partitioned approach offers more flexibility in solving the equations, but the need for an iteratively coupled exchange of information between the systems can often have negative effects on the stability and convergence of solutions. The papers by Veldman et al. [35, 36] give an idea as to why it is useful to find a middle-ground between these two methods, i.e., a method which has the robustness of the monolithic approach, without sacrificing the flexibility of the partitioned approach. In this thesis, we exclusively look at partitioned methods, first introducing a standard iterative coupling method, which is then compared to the more efficient, quasi-simultaneous coupling method.

To describe the partitioning of the numerical model, let us split the system into *solid* and *fluid* components, to discuss the dynamics over each. For the solid mote, we can use the simple force equation to describe its motion,

$$m_s \ddot{\mathbf{x}}_s = \mathbf{f}_{f \rightarrow s}, \quad (24)$$

and in a similar manner, the dynamics of the fluid can be described by

$$m_{ad} \ddot{\mathbf{x}}_f = \mathbf{f}_{s \rightarrow f}, \quad (25)$$

where the added mass, m_{ad} , is given in terms of the fluid resistance to the acceleration $\ddot{\mathbf{x}}_{fl}$.

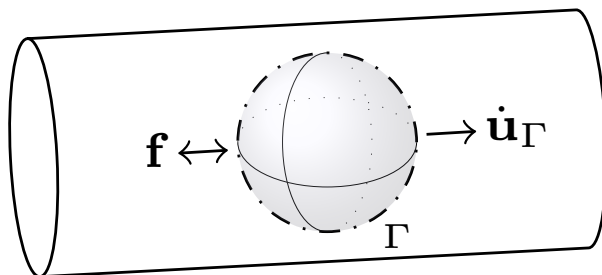


Figure 5: Motion and force conditions must be satisfied at the solid-fluid boundary, Γ .

The third relation to look at is the physical assumption that at the shared boundary, the fluid and the mote share characteristics, as mentioned in Section 3. This represents the necessary information exchange between the domains, such that we require

$$\mathbf{u}_s = \mathbf{u}_f, \quad \dot{\mathbf{u}}_s = \dot{\mathbf{u}}_f, \quad \text{and} \quad \mathbf{f}_{s \rightarrow f} = -\mathbf{f}_{f \rightarrow s} \quad (26)$$

along the shared solid-fluid boundary, Γ . This describes the intuitive assumption that the velocities and accelerations of solid and fluid particles should be the same at the interface, due to the no-slip

condition, and that the forces imparted from one to the other should subscribe to Newton’s Third Law.

Eqs. (24), (25) and (26) show the dynamic and kinetic constraints that we would like to impose (pointwise) on the model. However, given that the solid dynamics are governed by fluid forces over the entire surface, we can write this constraint in the operator form

$$\dot{\mathbf{u}}_{\Gamma} = Dp_{\Gamma}, \quad (27)$$

where D is the operator describing the dynamics of mote, therefore including the integration of the fluid pressure over the entire surface.

Similarly, we have explained that the fluid also reacts to the force of the mote, so we can write this in terms of an added mass operator, M_{ad} , such that

$$p_{\Gamma} = -M_{ad}\dot{\mathbf{u}}_{\Gamma}. \quad (28)$$

Although it appears that Eqs. (27) and (28) could be solved monolithically, this may not be the case due to the complexity of the system being modelled. For this reason, we will continue only with the partitioned approach.

4.2 Numerical methods

The standard way to use a segregated approach to solve a coupled system is to iteratively use one value to calculate the other, then use this new value to update the previous one. In this case, we would use the boundary fluid pressure, p_{Γ}^{old} , to determine the translation of the solid body, using

$$\dot{\mathbf{u}}_{\Gamma}^{new} = Dp_{\Gamma}^{old}. \quad (29)$$

From here, we would then calculate the new pressure field reacting to the movement of the body, which acts as a boundary condition within the Navier-Stokes equations, such that

$$p_{\Gamma}^{new} = -M_{ad}\dot{\mathbf{u}}_{\Gamma}^{new}. \quad (30)$$

Combining these two equations, we find the *weakly coupled* iterative scheme depicted by Fig. 6,

$$p_{\Gamma}^{new} = -M_{ad}Dp_{\Gamma}^{old}. \quad (31)$$

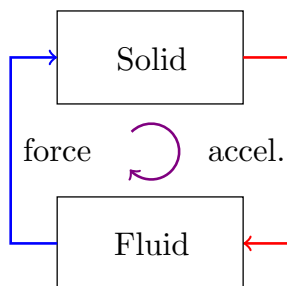


Figure 6: The weakly coupled iterative scheme.

Eq. (31) links back to Section 3.3, where we stated that for standard iterative methods there is a reliance on the ratio between the added mass and the solid body mass. It is a classical result

of iteration methods [21], that convergence will occur if the spectral radius of the iteration matrix satisfies

$$\rho(M_{ad}D) < 1, \quad (32)$$

where ρ denotes the *spectrum* of the operator. We have already seen that M_{ad} represents the added mass, but it is also true that D is inversely proportional to the mass of the solid body. Therefore, this spectral property finds a condition for the ratio of the added mass to the body mass, as stated by Eq. (23).

This is not to say that if $\rho(M_{ad}D) \geq 1$ then we cannot proceed; instead, we take note that convergence can be achieved by utilising a sub-iterative scheme of under-relaxation, which greatly adds to the computational work. This is obviously not ideal for computational models, and so a new approach is preferred, one which can be as close as possible to a monolithic method, while still retaining the flexibility of segregated methods [35, 36].

To avoid the inclusion of costly sub-iterations, instead of relying on the complete fluid dynamics, represented by D , we instead use a good enough approximation, denoted \tilde{D} , which is still able to be used as a boundary condition in the Navier-Stokes equations. We then define a new *interaction law*

$$\dot{\mathbf{u}}_{\Gamma} = \tilde{D}p_{\Gamma} \quad (33)$$

which will be incorporated into the solution of the system [33]. The time integration process to solve the coupled system can then be described by the *quasi-simultaneous* iterative coupling scheme:

$$\begin{aligned} \text{Interaction Law :} & \quad \dot{\mathbf{u}}_{\Gamma}^{new} - \tilde{D}p_{\Gamma}^{new} = (D - \tilde{D})p_{\Gamma}^{old} \\ \text{Navier-Stokes B.C. :} & \quad p_{\Gamma}^{new} + M_{ad}\dot{\mathbf{u}}_{\Gamma}^{new} = 0. \end{aligned} \quad (34)$$

Ignoring technical details, this new scheme works in such a way that the fluid ‘anticipates’ the reaction of a solid body to pressure forces, rather than relying on standard back-and-forth computations.

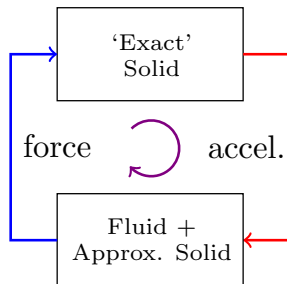


Figure 7: The quasi-simultaneous coupling scheme.

Combining Eqs. (34) to eliminate the acceleration term, we are then left with

$$(I + M_{ad}\tilde{D})p_{\Gamma}^{new} = -M_{ad}(D - \tilde{D})p_{\Gamma}^{old}. \quad (35)$$

The usefulness of this new iteration scheme lies in the fact that even if the added mass operator is large, convergence can still occur when \tilde{D} represents D closely, therefore removing the reliance on costly sub-iterations. A more technical overview of the quasi-simultaneous method can be found in [33], and for more technical results, consult [35, 36].

5 Computational Results

5.1 Discretization of the geometry

Before discussing the numerical differences between the weakly coupled iterative method and the quasi-simultaneous coupling method, we must first describe the computational geometry of the model.

Looking at qualitative behaviour of the solid-fluid system meant that we could make certain assumptions, the first of which being that the pipe being modelled is symmetric about its cylindrical axis. Because of this, the initial models were represented in only two dimensions, allowing us to gain a general understanding of the system behaviour, without the need for computationally-heavy three-dimensional simulations. It was agreed that should the 2D models not agree with 3D expectations, then the simulation set-up would be changed, but fortunately this did not happen.

Three different pipe geometries were used for the simulations, albeit only differing in length, and two different mesh sizes were utilised, depending on the investigations being performed⁶. Details of the different set-ups are given in Section 9.1, with the standard geometry being shown in Fig. 8. It is worth mentioning that although we describe the model in terms of *metres*, this is only to give some kind of physical reference to the reader. Instead, the physical dimensions in the model are all scaled with respect to one another, so results can be realised as *relative* results, rather than ones tied to a specific geometric scale.

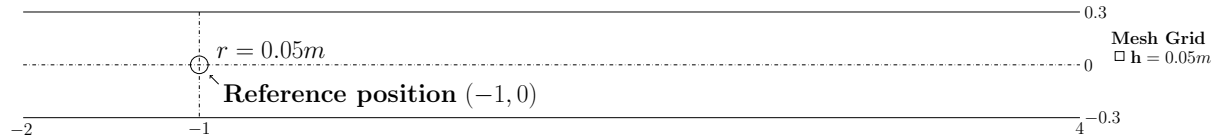


Figure 8: The standard geometry of a $6m \times 0.6m$ two-dimensional pipe, with a mesh of 120×12 .

With respect to the mote, we modelled it to be symmetric, with uniform density, such that it had a symmetric centre of mass, reinforcing our assumption of a symmetric model⁷. However, in talks with INCAS³ we later found out that the WiseMotesTM do *not* have a symmetric centre of mass, which seemingly affected some of their experimental data. That said, these initial simulations were designed to understand the overall behaviour of the motes, and so it was assumed that, from a qualitative standpoint, the simulations still reflect the general physical behaviour.

All simulations were completed using *ComFLOW 4.0.1*, a program for the numerical simulation of fluid flow, based on the Navier-Stokes equations, developed at the University of Groningen.

5.2 Results

5.2.1 Initial vertical position

The first parameter to be discussed is the initial height position of the mote, i.e., *What effect does a change in initial vertical position have on the trajectory of the mote?*⁸. Fig. 9 shows the trajec-

⁶It is important to note that *both* of the grids used in this study were coarse, however, one had four times the number of cells. For this reason, we will refer to the grids as ‘coarse’ and ‘fine’, even though neither of them is *fine* in a technical sense.

⁷As we were working in a two-dimensional environment, the sphere was actually replaced by a cylinder within the models, due to the fact that a sphere could not be defined in a 2D framework.

⁸Note that we use the term *vertical* position with respect to the pipe’s centre axis. This is for convenience, as the parameter actually represents the radial distance from the centre axis in three dimensions.

jectories for nine different simulations, each with a starting vertical height of $y = 0.03h$ metres, for $h = 0, \dots, 8$.

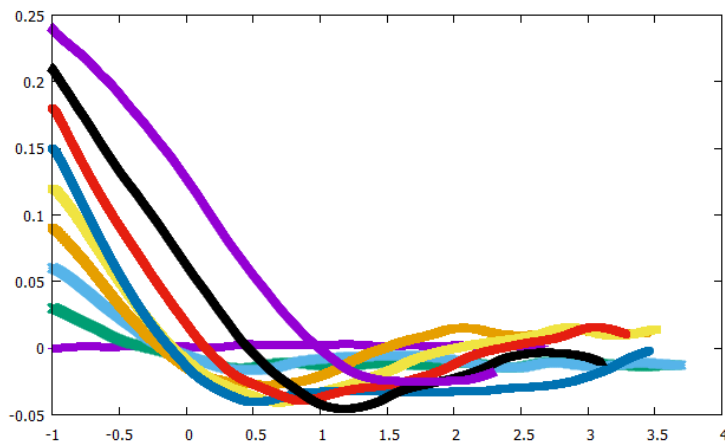


Figure 9: Plot of mote trajectories from different initial heights.
Grid: 240×24 . Time: 15 seconds.

This set of simulations was run with a mote of radius $r = 0.05m$, with a solid density of $\rho_s \approx 20$, and a baseline fluid density of $\rho_f = 1$. Gravitational effects were removed from the model, meaning that the large solid density did not have any kind of asymmetric effect on the resulting trajectories. The pipe geometry was taken to be $8m$ long (in case any simulations ran further than expected), and $0.6m$ tall, over a square grid with a mesh width of $h = 0.025m$.

It is relatively clear that the trajectories seem to converge to the middle of the pipe, around the point $y = 0$, well within a range of $\pm 0.05m$. Although the simulations were run on a *technically* coarse grid⁹, the behaviour agrees with initial experimental observations made by INCAS³, in which motes released in controlled laminar flow would converge towards the centre of the pipe.

Physically speaking, there are multiple forces that are felt by the motes, so it is important to discuss results with respect to the following:

- **Wall-induced lift:** For off-centre motes, the impact of the pipe wall may cause a *local* disturbance in the flow field, which could create a non-negligible, asymmetric wake around the mote; this would have the effect of causing the mote to tend towards the centre of the pipe. The actual wall effects are not simple to analyse, but from a purely qualitative standpoint, this effect should occur in principle.
- **Rotational forces:** Due to the Poiseuille velocity profile, the ‘top’ and bottom’ of the mote will experience different flow velocities, creating a rotational effect about the mote’s centre of mass¹⁰. Due to these rotational effects, we may find a *Magnus force* acting on the mote, which

⁹It would be useful for the reader to understand that simulations were run on coarse grids for multiple reasons. One reason is that the amount of time available for simulations was not very long, so it was deemed more prudent to run many simulations on coarse grids, rather than few simulations on a finer grid. Secondly, the focus of this project was to determine qualitative behaviour, rather than find extremely detailed results, so the use of coarse grids meant that general behaviour could be observed without the need for heavy computational effort. Finally, the simulations described in this study were all run on an Acer Aspire 5750 (2011 model) – a consumer-grade laptop which, in all likelihood, is not built to withstand intensive CFD simulations.

¹⁰Recall that the simulated motes are assumed to have uniform density, and therefore a symmetric centre of mass. This is *not* exactly how the current WiseMotesTM have been constructed, so *actual* rotational effects will be more complex.

in the system we are studying would also cause the mote to travel towards the centre of the pipe.

- **Shear-induced lift:** Again, due to the Poiseuille profile, it may be that the motes experience a lift which acts in the direction of the pipe wall, countering the inward-directed forces; the reason for this is due to the interaction of the wake and the velocity profile of the flow. This effect occurs in microfluidic systems [24, 25, 23], causing particles to migrate from the centre axis, but as the simulations are run in terms of *scaled* dimensions, this effect may also exist within our model.

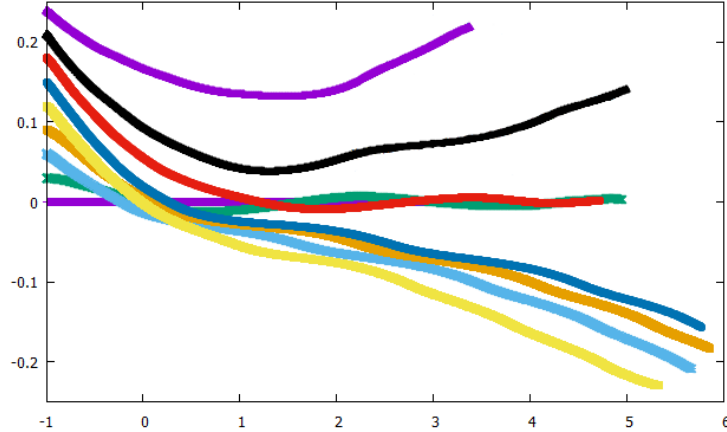


Figure 10: Plot of mote trajectories from different initial heights.
Grid: 120×12 . Time: 15 seconds.

To try to find a hierarchy of how important each force is, we can look at the set of almost-identical simulations which were computed over a 120×12 grid, i.e., the number of grid cells is halved in both directions. Fig. 10 shows the trajectories of these nine simulations, and it is very clear that the behaviour compared to Fig. 9 is almost entirely different. There still appears to be a range of equilibrium around the centre axis, but now it appears to be a lot less stable. Not only do we find that just three of the motes tend towards to the centre of the pipe, one of which being the reference simulation with $y_0 = 0$, but the remaining six motes show behaviour that is in direct disagreement with the experimental findings of INCAS³.

One way to interpret this discrepancy would be to assume that on the fine grid we are indeed depicting a more accurate representation of real-life flow behaviour¹¹. This would suggest that any forces that exist in the coarse model which cause the divergent trajectories are in fact overpowered by more important forces in the more accurate model. From the three forces mentioned previously, this would suggest that the wall-induced lift and the possible rotational effects are intrinsic to the behaviour of the mote trajectories, and so the finer grid represents these forces more accurately. However, the relative strengths of such forces cannot be ascertained from these simple models, but there have been many involved studies to try and determine such forces acting on spherical particles [38, 39].

It is worth noting that there are many articles that focus on the *inertial migration* of spheres in pipes and channels, both neutrally and non-neutrally buoyant, most of which build upon the pioneering work of Segré and Silberberg [24, 25], and their finding of the *Segré-Silberberg effect*. This

¹¹This seems likely, as in the coarse simulations the mote is the size of a *single* grid cell.

initial experimental study, which was actually a modern set-up of observations made by Poiseuille in the 1830s [20], found that small, spherical particles in a suspension tended towards a non-central equilibrium distance of around $0.6R$, where R was the radius of the tube. This result has been confirmed in numerous other studies [11, 23, 38], and theoretical explanations have also been attempted [10]. A computational study by Feng et al. [9] was able to model slightly larger macroscopic spheres, finding that the *Segré-Silberberg effect* still existed in these models, attributing the forces to wall repulsion, a shear-induced inertial lift, and a rotational lift. These findings not only agree with the assumptions that were made on the previous page, but they also reiterate the fact that internal pipe forces are certainly not simple to calculate.

This said, there are not many studies that focus on spheres of the size being used by INCAS³, so it may in fact be that the observed effects are diminished in larger, industrial pipelines. Also, given the coarseness of the grids that were used in the simulations, any deeper interpretations should be left until after a grid-refinement study. Most of the studies referred to used flows with very low Reynolds numbers; interestingly, on these coarse grids the *effective* Reynolds number may in fact be lowered so much that these quantitative effects are observable in our simulations, while not necessarily existing in the real flow we are trying to model.

Regardless, it is interesting, and somewhat rewarding, that the computational models agree with the experimental findings of INCAS³, even if they do not fully match other experimental observations. From our specific force assumptions, it would therefore be reasonable to suggest that any outward-directed forces that exist in the system have a much weaker effect than the combination of any inward-pointing forces.

5.2.1.1 A simple mistake

Up to this point, the argumentation and description of the models has been valid, however there is one caveat of the results that must be explained. For all simulations that were run using this version of *ComFLOW*, there was a mistake in the code relating to the direction of shear forces, and therefore the results may be somewhat inaccurate. Sadly, the error was discovered too late in this project’s timespan, but a single set of repeated simulations were able to be run, to compare the previous trajectories to the (hopefully) accurate ones; these results are shown in Fig. 11.

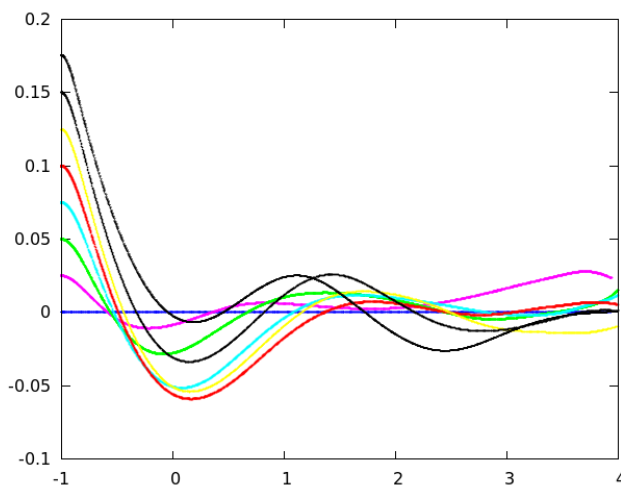


Figure 11: Mote trajectories using the revised *ComFLOW* code, using initial heights of $y_0 = 0.025h$, for $h = 0, \dots, 7$.

Although the simulation set is not exactly the same, using only eight different initial positions, the general behaviour of the motes appears to be near identical to what we found previously in Fig. 9. One thing that is very interesting though is the behaviour of the mote released at $y_0 = 0.025m$ (pink trajectory), which tends towards the centre-axis of the pipe, only to diverge slightly around the $2.5m$ mark. This *could* be a hint that the *Segré-Silberberg effect* will have some sort of an impact on these computational models, finding that motes may indeed tend to non-central equilibria.

Unfortunately, this project was not long enough to perform detailed, long-term simulations, but hopefully these initial data sets provide a useful foundation for any future projects, or further experimentation.

5.2.2 Increasing mote radius

The second investigation directly related to INCAS³ had a focus on the radius of the mote, i.e., *What effect does a change in mote radius have on the behaviour of the fluid flow?* This problem is important for two reasons:

- **Scalability:** INCAS³ needs to know whether using motes that were relatively large with respect to the pipe diameter would cause implementation issues, i.e., would a larger mote experience any problems that smaller motes might not?¹²
- **Flow disturbance:** INCAS³ wish to capture and analyse different types of data to determine the flow behaviour at a given point. However, if the mote has too much impact on the flow, then the captured data may not be representative of regular flow behaviour.

The computational geometry was the same as shown in Fig. 8, using the same mote as in the previous study¹³ as a reference model, with simulations being run for a time interval of ten seconds. For the required comparison, simulations were run over radial values of $(0.05 + 0.01q)$ metres for $q = 0, \dots, 24$, using both types of iterative coupling methods. Whereas the previous investigation was primarily of interest only to INCAS³, this part of the study was also used to analyse the computational efficiency of using the quasi-simultaneous method, compared to the weakly coupled method.

As mentioned by Veldman et al. [35], the important factor to compare the two methods was not for how many total iterations the program was running, but instead how many *pressure equation sub-iterations*¹⁴ were required to be solved for the simulation to be complete. It has been noted that the weakly coupled method often has a much larger number of sub-iterations, and that this number is dependent on the amount of fluid being shifted by the mote, i.e., the added mass, m_{ad} [35, 36]. Therefore, this led us to expect that the number of pressure solves would increase as the mote radius increased, due to the mote disturbing a greater amount of fluid.

A plot of the total number of pressure solves on the coarse grid is shown by Fig. 12; it is clear that the quasi-simultaneous method indeed requires fewer pressure solves, and is therefore more computational efficient. However, the difference in computational load was certainly not as great as expected, so the same simulations were re-run on the fine mesh. This time, we only ran simulations for radial values of $(0.05 + 0.03q)m$ for $q = 0, \dots, 8$, in light of the increased computation time; results for this simulation are shown by Fig. 13.

¹²Although we talk about increasing the size of the mote, in the numerical model this has the same effect as reducing the diameter of the pipe. INCAS³ *technically* wanted to see the behaviour of motes in various pipe diameters, as the WiseMotesTM have a predetermined size. However, if we were to instead alter the size of the pipe in each simulation, then we would either have to increase the number of grid cells, making the computation time longer, or we could keep the same number of grid cells, but make the grid more coarse. For this reason, we decided to choose the size of the mote as the variable, such that the model geometry could stay the same for each simulation.

¹³ $r = 0.05m$, $\rho_s \approx 20$.

¹⁴Referred to throughout this thesis as 'pressure solves'.

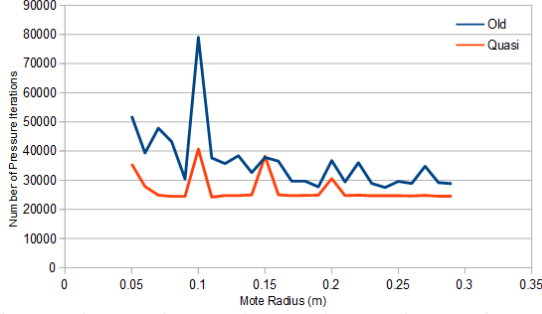


Figure 12: Total number of pressure solves, for increasing radius values. Grid: 120×12 .

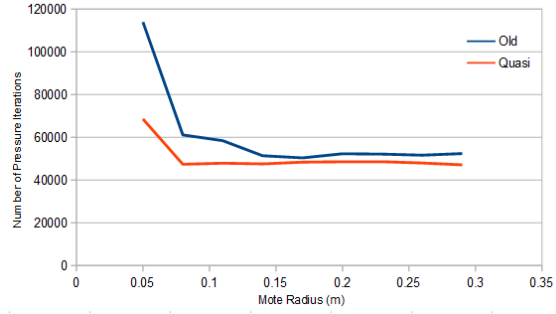


Figure 13: Total number of pressure solves, for increasing radius values. Grid: 240×24 .

The two plots show that there tended to be an average difference of 4000 to 10000 pressure solves between the two methods, when much more complex simulations had shown a huge disparity in computational effort [35]. To understand the reason for this, we can look at the added mass plots for the two simulation groups, shown by Figs. 14 and 15¹⁵.

The relation between the decreasing added mass ratio and the total number of pressure solves is obviously clear, yet it still did not explain why the results were not as expected; the results should have represented a causal relationship between the *increase* in the mote radius, and an *increase* in the added mass ratio. As explained before, this comes from the notion that as the mote size increases, it will be impacting on more fluid within the pipe, and so the amount of added mass increases.

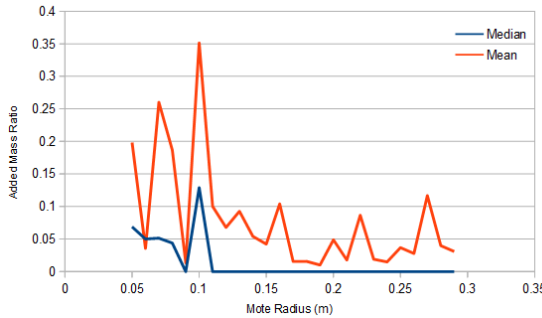


Figure 14: Median and mean added mass ratio. Grid: 120×12 .

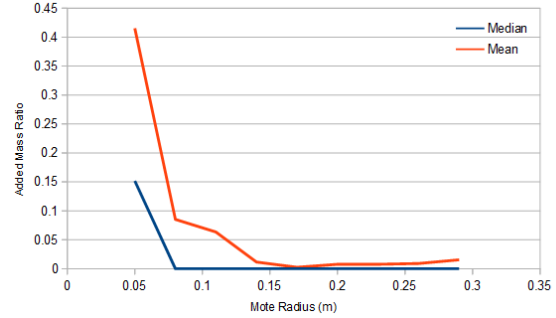


Figure 15: Median and mean added mass ratio. Grid: 240×24 .

What these results seemed to indicate was that as the mote increased in size, the amount of fluid being shifted was not increasing. This thought is not entirely correct though, as the plots do not represent the total fluid mass being shifted, but rather the *ratio* of that mass with respect to the mass of the mote. As the radius of the mote increases, the mass of the mote increases quadratically¹⁶

¹⁵Note that the added mass ratio is plotted *only* for the weakly coupled method, because the added mass ratio does not affect the quasi-simultaneous method, as explained at the end of Section 4.2.

¹⁶The increase is quadratic here, as the mote was modelled as a cylinder. For simulations that actually use a sphere, the growth will be cubic. It may be worth mentioning here that the added mass over a cylinder is calculated to be $\rho\pi R^2 L$, where R is the cylinder radius, and L is the length. This means that the cylinder has a *relatively* greater added mass compared to a sphere.

to maintain the same density, so these results appeared to show that the increase in the amount of fluid mass being disturbed by the mote was not enough to offset the increase in mote mass.

Thinking about the parameters of the model, it seemed likely that perhaps the density of the mote was too large to find any meaningful results. Originally, the reference models had been made with a mote density far greater than that of water, but for the previous investigation this had not had any impact on the outcome of the simulations as gravitational effects were ignored. Here, however, there is a direct relation between the reference mass of the mote, and the expected results, so by using the same reference model as before, we had ultimately skewed our results.

The next step was obvious; change the density of the mote such that it was equal to the density of the fluid, i.e., $\rho_s = \rho_f = 1$. This meant that the models would describe the *neutrally buoyant* motes that INCAS³ were experimenting with, and so they would also be more representative of the computation load that would be undertaken in more realistic analyses. The same set of simulations were then run, and the resulting pressure solves data is shown by Fig. 16.

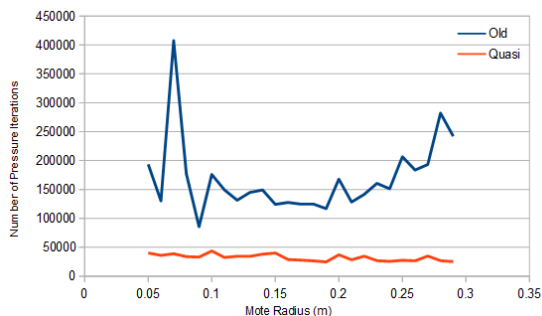


Figure 16: Total number of pressure solves, using a neutrally dense mote. Grid: 120×12 .

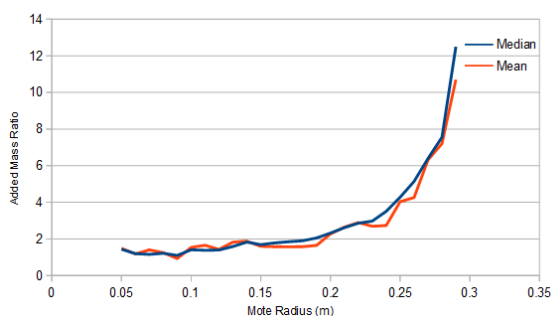


Figure 17: Median and mean added mass ratio, using a neutrally dense mote. Grid: 120×12 .

These results represent our expectations a lot more closely, with the average computational difference being over 100,000 pressure solves. Apart from the spike at the left-hand side, which can be treated as an anomaly, the weakly coupled method also agrees with the assumption that the number of computations would increase, due to the larger amount of fluid being disturbed by the mote. The relation to the added mass of the fluid is even more apparent when compared to Fig. 17. Together, these results confirmed our expectations, not only about the behaviour of the fluid with respect to an increasing mote, but also how well the quasi-simultaneous coupling method would perform within this FSI model.

Finally, given that the Fig. 17 shows only the median and mean values of the entire data set, Fig. 18 shows the full data distributions for $r = 0.05m$ (black), $r = 0.2m$ (violet), $r = 0.23m$ (orange), $r = 0.26m$ (blue), and $r = 0.29m$ (red). This plot shows that the added mass ratios were highly consistent, so the weakly coupled method is affected from the very beginning of the simulation, meaning that the quasi-simultaneous coupling method does not require any initial amount of time to *become* more efficient, it just simply *is* more efficient. Simulations were also run over the finer grid, again using radial increments of $+0.03m$ rather than $+0.01m$, with the results being grouped in Section 9.2.

In terms of physical analysis, the simulations of increasing mote radius did not give too much detail about *how* the fluid flow is actually affected when the relative radius becomes larger. The simulations showed that there were large pressure increases behind the mote, which was expected, but

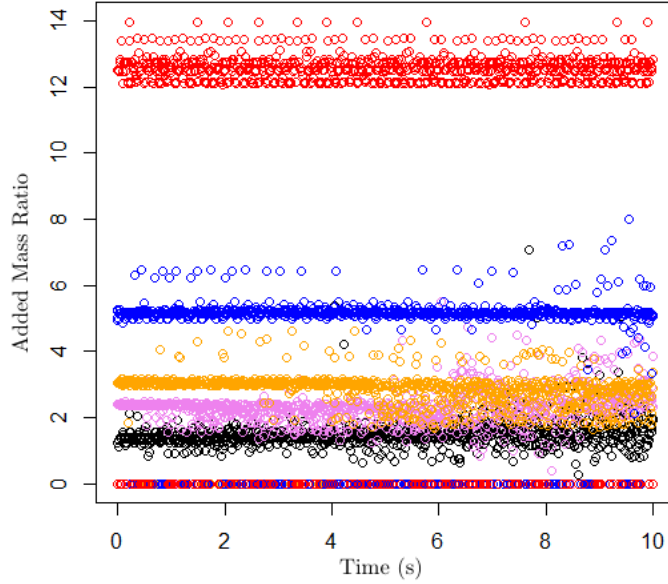


Figure 18: Distributed added mass ratios for multiple data sets, using the coarse grid.

due to the symmetrical nature of the model, these had a negligible impact on the flow trajectory. For this study, it was decided that a cross-examination of both radial changes *and* initial height changes was unnecessary, as it would take too much time to create a data set large enough to find meaningful results. However, for INCAS³, this may well be where some important information lies, as we may find that there are forces that become more apparent, such as larger rotational forces for larger motes, when released off-centre. Again, hopefully this initial study will provide a platform for more in depth investigations to be carried out in the future.

5.2.3 Initial horizontal position

The final investigation was to determine the effect of shifting the horizontal position of release for the mote, by moving it closer to the inlet flow. This did not have any direct impact on the INCAS³ project though, as we had chosen the flow profile to be fully-defined at the beginning of the simulation. Therefore, the behaviour of the mote would *in theory* be the same if it were released at the start of the pipe, or the middle of the pipe¹⁷. Instead, this study was used to further confirm the usefulness of the quasi-simultaneous method to solve this type of coupled system, over a standard iterative method.

The model geometry for these simulations was reduced to only four metres, as there would be no need to have grid cells in an area of the pipe that the mote would never reach. Also, the radius of the mote was taken to be $r = 0.1m$ for these simulations, and both the solid and fluid densities were kept at a value of $\rho = 1$. The set-up of the investigation was simple; move the mote closer to the inlet boundary of the geometry, and monitor the number of pressure solves needed to find a solution. Fig. 19 shows the points of release that were investigated for this part of the thesis.

¹⁷We use the clause ‘in theory’, because a change in initial conditions will understandably change the very nature of the flow. However, it was assumed that unless the computations were unable to be completed, the computed flow behaviour would be near-identical no matter where the horizontal start position was.

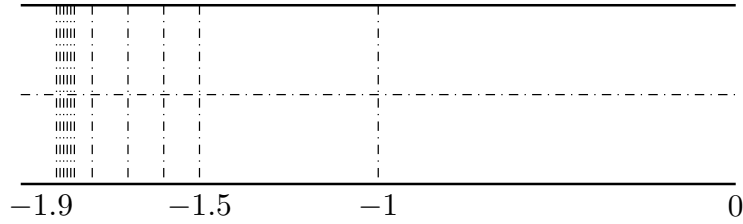


Figure 19: Horizontal release points of the mote;
 $x = \{-1, -1.5, -1.6, -1.7, -1.8, -1.85, -1.86, -1.87, -1.88, -1.89, -1.9\}$.

Figs. 20 and 21 show the number of pressure solves, and the added mass ratio averages for each of the simulations. The impact of moving closer to the inlet flow is relatively clear, as the number of pressure solves seems to slowly increase as the mote gets closer to the geometry inlet¹⁸. However, there is clearly not the same type of behaviour as we saw for the radius investigation.

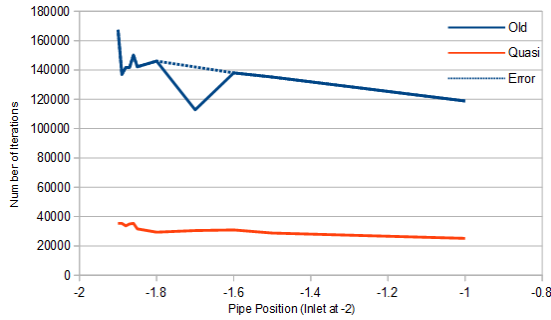


Figure 20: Total number of pressure solves, moving closer to the inlet flow. Grid: 120×12 .

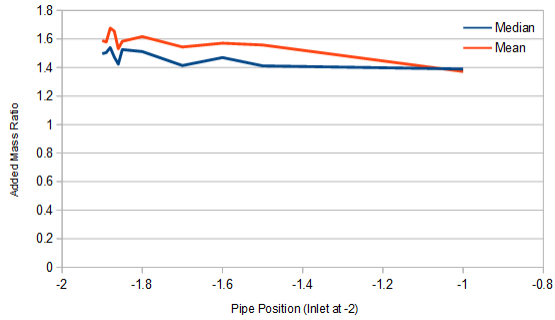


Figure 21: Median and mean added mass ratio, moving closer to the inlet flow. Grid: 120×12 .

The expectation of a greater computational load did not come from an increase in mass this time, but rather in the expected difference in velocities and pressures of the solid and the fluid. When the simulation begins, the mote is immediately introduced to the system, with zero initial velocity. Given that we take the Poiseuille field to be fully-formed, this means that at the boundary of the mote there will be an immediate discontinuity of velocities. Both numerical methods are able to combat this problem, but it was expected that as the mote moved closer to the inlet flow, there would be more computations to settle the imbalance. Note that this does not come from the fact that the flow becomes faster as the mote approaches the inlet, but rather that the *gradient* of the velocities will become much steeper, due to the narrowing gap. Similarly, the immediate pressure differences between the solid and the fluid would also cause a greater computational load as the release point moved towards the inlet, due to the sharper pressure gradient.

With this in mind, we still had the expectation that the quasi-simultaneous coupling method would outperform standard methods, due to the fact that at each iteration the fluid ‘anticipates’ the reaction of the solid body. These results obviously confirm our expectation that the quasi-simultaneous method is a lot more efficient, by a factor of between 3 and 4 in these coarse simulations. What

¹⁸The sudden drop in Fig. 20 occurred because the simulation was unable to be completed, due to problems with the convergence of a pressure solution. However, because later simulations *did* complete, we treated this point as an anomaly.

is also interesting is that as the release position gets closer to the inlet boundary, the number of standard pressure solves become slightly skewed, as shown by Figs. 22 and 23.

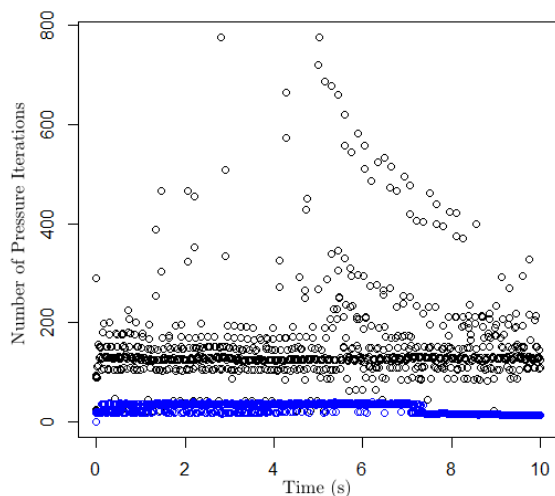


Figure 22: Distribution of pressure solves, using the release point $x = -1.0$. Grid: 120×12 .

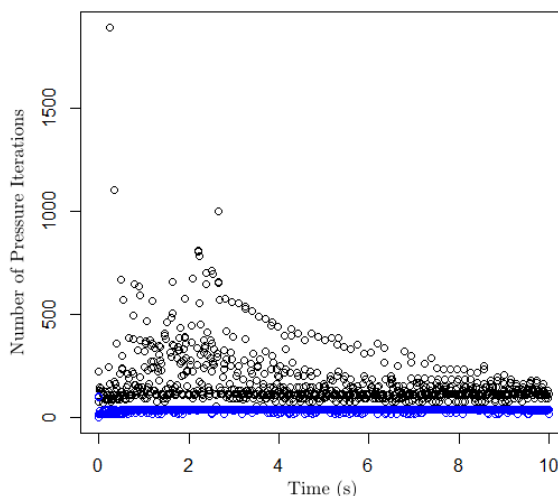


Figure 23: Distribution of pressure solves, using the release point $x = -1.9$. Grid: 120×12 .

These figures show that the quasi-simultaneous method (blue) is consistent in how many pressure solves it must compute at each time step, thanks to the anticipation factor, while the weakly coupled method (black) becomes positively skewed, suggesting that it requires *more* solves for the earlier computations, due to the sharper pressure differences. This means that the quasi-simultaneous method is a more useful coupling method for FSI models such as these, as the coupling between the fluid and the solid is dealt with in such a way that computational effort is barely increased for set-ups which could otherwise cause serious numerical issues.

5.3 Summary of numerical simulations

The results that were gained from this investigation agreed closely with the expectations that we had (once the physical parameters had been reasonably defined). The results from the initial height simulations match early observations obtained by INCAS³ from experimental set-ups, which is hopefully a sign that mote behaviour *can* be modelled accurately using *ComFLOW*. Any progression from these qualitative models would need to account more fully for the inertial effects of the fluid on the mote, and perhaps more detailed experiments would need to be performed, either to set expectations, or to confirm model predictions.

Similarly, the effect of slimmer pipelines should be investigated experimentally, to understand what effect the mote actually does have on the surrounding fluid, and whether the increase in pressure affects the regular behaviour within the pipe. This could then be compared against more detailed computational models, especially ones which investigated the effects of *combined* parameter changes. This was understandably beyond the scope of this project, not in terms of content, but rather in terms of available time.

Given that INCAS³ wishes to utilise both neutrally and non-neutrally buoyant motes, it would be interesting to explore the modelled effects of different mote masses, in a more controlled way than we did in this study. If possible, it could also be useful to mimic the correct centre of mass of the WiseMotesTM, such that any rotational effects are modelled more accurately. However, this

study aimed to find qualitative behaviour patterns of the notes, and it has certainly opened the initial gateway to the numerous investigations that can be continued from this point.

Aside from this, we also aimed to validate the efficiency of the quasi-simultaneous coupling method, and this has definitely been shown. In the *realistically* defined models, the quasi-simultaneous method lived up to expectations and simulated the models with much greater speed than the standard iterative method. This thesis should serve as a recommendation for the use of the quasi-simultaneous coupling method in other FSI models, particularly any studies which continue from this one.

6 Port-Hamiltonian Systems

The segue from computational modelling into port-Hamiltonian systems may not seem like an obvious choice, yet it is born from a few basic assumptions that are shared between the two disciplines:

- **Multiple physical domains:** The problem underlying this thesis is, in simple terms, focused on coupling the equations from two different domains; the domain of the solid mote, and the domain of the fluid in the pipe¹⁹. In the computational model, the difficulty lies in solving the necessary sets of equations together, in such a way that both are satisfied. In comparison, port-Hamiltonian systems can be used to describe systems with multiple components, whereby we now focus on trying to couple the two domains analytically, such that certain constraints are satisfied.
- **Shared physical characteristics:** The formulation of the previous work, both analytically and computationally, was built on the assumption that at the shared solid-fluid boundary, the dynamic and kinematic properties would be in unison, i.e., the velocities and accelerations would be equal, and the forces would be negatives of one another. This seems to mirror a key property of port-Hamiltonian systems, whereby we require a certain *power balance* at the interface of different system components, where power is given by the product of different physical variables.

6.1 Prerequisites

The language of port-Hamiltonian systems is far removed from anything discussed so far, so we present some *very* basic explanations of the fundamental concepts, which will be vital to representing this problem in such a framework. For a broader understanding of port-Hamiltonian systems, the reader is pointed in the direction of works by van der Schaft, namely [29] and [31].

6.1.1 Hamiltonian mechanics

In Hamiltonian mechanics, the time evolution of a system is governed by a *Hamiltonian*, $H(\mathbf{q}, \mathbf{p}, t)$, and the equations

$$\begin{aligned}\frac{d\mathbf{q}}{dt} &= \frac{\partial H}{\partial \mathbf{p}}, \\ \frac{d\mathbf{p}}{dt} &= -\frac{\partial H}{\partial \mathbf{q}},\end{aligned}\tag{36}$$

where (\mathbf{q}, \mathbf{p}) are the *canonical coordinates*²⁰, and t is time. In most systems, the Hamiltonian is taken to be the sum of the kinetic and potential energy of the system, but it is *not* necessarily required to be.

Hamilton's equations (36) can be derived from the *Lagrangian* of a system, i.e., the kinetic energy *minus* the potential energy; this derivation can be found in most undergraduate physics textbooks [15]. This is then often followed by *principle of least action*, a variational principle that can be applied to the *action* of a mechanical system to find the equations of motion. We will not go into details here, but instead stress that for many mechanical systems there is a well-structured procedure that can be followed, culminating in Hamilton's equations.

Alternatively, we could also describe Hamiltonian dynamics in a more abstract way, taking the

¹⁹Rather than treat the pipe wall as a separate solid domain, we instead regard it only as a boundary condition on the fluid domain.

²⁰We call \mathbf{q} the *generalized displacement*, and \mathbf{p} the *generalized momentum*.

Hamiltonian as a real-valued function defined over a phase space, \mathcal{X} . We can view the phase space to be all possible configurations of the canonical coordinates, e.g., for a single moving particle there are *six* degrees of freedom (three translational, three rotational), so the phase space is a six-dimensional manifold, \mathcal{X}_6 , which may or may not be equal to \mathbb{R}^6 . We can then take the Hamiltonian to represent the total energy of the particle, with $H : \mathcal{X} \rightarrow \mathbb{R}$, such that each point in the phase space has a distinct energy associated with it. By viewing the phase space as a manifold, we can make use of concepts such as tangent planes, tangent spaces, and dual spaces, which have specific representations in the evolution of a system. However, in our case we will be using a state space that is equal to some n -dimensional (possibly infinite) lattice \mathbb{R}^n , with no fundamental requirement to use an abstract manifold.

With this said, we urge the reader to understand that a Hamiltonian viewpoint can often be very useful in understanding dynamical systems. Many people find that the use of a Hamiltonian formulation allows a larger, unifying framework to be described, to be used as a benchmark to compare more detailed systems against. Other times, it can be useful to analyse the geometric construction of Hamilton's equations, which state that a system evolving through time is equivalent to flowing along a vector field on the phase space. A Hamiltonian framework often finds explicit mathematical symmetries (not necessarily *physical* symmetries), which are otherwise hidden in Newtonian or Lagrangian forms. While Hamiltonian mechanics is essentially a reformulation of classical mechanics, it usually allows the user to see a system from a different perspective, or to explore fundamental ideas about generalized systems of a certain type.

6.1.2 Port-Hamiltonian definitions

Port-Hamiltonian systems theory builds on the perspective of *port-based modelling*, a framework developed in the 1950s that allowed multi-physics systems to be analysed as a whole, using *energy* as the currency shared between each physical domain [19]. More specifically, port-Hamiltonian systems have a deep connection to *systems and control theory*, stressing the importance for dynamical systems to be able to interact with their environment, or to even be open to a certain amount of user-defined control. This aspect will not be explored in this thesis, as the focus will primarily be to understand how to represent the solid-fluid coupling with this new methodology. This subsection will be a brief introduction to port-Hamiltonian systems, outlining the most important concepts to then apply them to the FSI system.

The basic set-up of a port-based model is to regard the system as an interconnection of three types of ideal elements:

- *Energy-storing* components, such as inductors, springs, and masses
- *Energy-dissipating* components, such as resistors, and dampers
- *Energy-routing* components, such as transformers, and gyrators

In a port-Hamiltonian framework, all storage elements are usually grouped into a single object²¹, denoted \mathcal{S} , and similarly all dissipating components are grouped into the *resistive* object \mathcal{R} . To connect the system, the energy-routing elements are combined into a single energy-routing structure \mathcal{D} , known as a *Dirac structure*. A depiction of a general port-Hamiltonian system, connected to some kind of external environment, is shown by Fig. 24.

As shown in the depiction, the interconnection of the system is governed via pairs (f, e) , which are (pairwise) equal-dimension vectors of *flow* and *effort* variables²². For reasons which will be

²¹In this thesis, we treat the two storage elements, the solid and the fluid, as *separate* energy-storing elements, for clarity of explanation.

²²We may also refer to them generally as *port variables*, or refer to the pair (f, e) as a *port*.

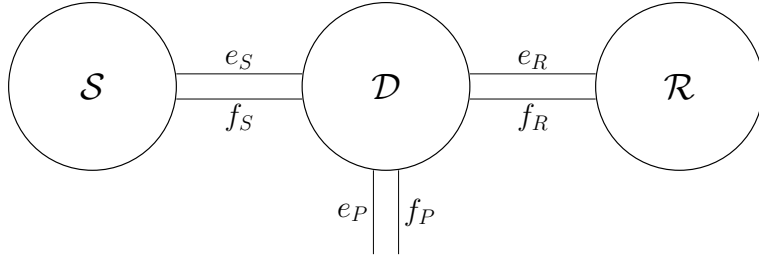


Figure 24: The structure of a port-Hamiltonian system, connected to a general environment \mathcal{P} .

explained, these pairs are often called *power variables*, due to the fact that they are defined in such a way to make the inner product, $e^T f$, have the same dimensions as *power*;

$$[e^T f] = \text{kgm}^2 \text{s}^{-3}. \quad (37)$$

Thus, in Fig. 24, the scalar quantities $e_S^T f_S$, $e_R^T f_R$, and $e_P^T f_P$ respectively represent the instantaneous power transmitted in (or out) of the storage element, the resistive element, and the environment, *through* the energy-routing element, \mathcal{D} .

The object \mathcal{D} is pivotal in the structure of a port-Hamiltonian system, and has the property of conserving power within the entire system, i.e., the summation of the powers being transferred is equal to zero. A more formal definition can be found in [31], but the basic premise is as follows. Let us take a finite-dimensional linear space, \mathcal{F} , from which we take *flow vectors*, $f \in \mathcal{F}$. The space of *effort vectors* is taken to be the dual of \mathcal{F} , such that $e \in \mathcal{E} := \mathcal{F}^*$. Therefore the *power* is the total space of power variables defined by

$$P = \langle e | f \rangle, \quad (f, e) \in \mathcal{F} \times \mathcal{E}, \quad (38)$$

where $\langle e | f \rangle$ is the duality product²³.

We can therefore define a *Dirac structure* to be a subspace $\mathcal{D} \subset \mathcal{F} \times \mathcal{E}$ such that

$$\langle e | f \rangle = 0, \quad \text{for all } (f, e) \in \mathcal{D}. \quad (39)$$

There also exists a *maximality condition* which should be imposed, such that $\dim \mathcal{D} = \dim \mathcal{F}$, but this property is not required at any point in this thesis. The most important notion concerns the power balance described by Eq. (39). A greater overview of Dirac structures, along with extra properties and examples, can be found in [29, 30, 31]. However, the only other information that we need for now regards the description of *transformers* and *gyrators* in port-Hamiltonian language, specific ways to link two ports, which are also referred to later in this thesis.

A *transformer* is defined as an energy-routing element linking two *ports*, (f_1, e_1) and (f_2, e_2) such that

$$\begin{aligned} f_2 &= \alpha f_1, \\ e_1 &= -\alpha e_2, \end{aligned} \quad (40)$$

with α denoting the *transformer ratio*. The vector form is therefore

$$\begin{aligned} f^b &= A f^a, \\ e^a &= -A^T e^b, \end{aligned} \quad (41)$$

²³If we take $\mathcal{F} = \mathbb{R}^n$, then the duality product is merely the standard inner product.

where (f^a, e^a) and (f^b, e^b) are vectors pairs that (pairwise) have the same dimensions. In both cases, either scalar or vector, the linking element which constrains the equations does define a Dirac structure. In a similar way, a multi-dimensional *gyrator* is defined as

$$\begin{aligned} f^a &= Ge^b, \\ f^b &= -G^T e^a, \end{aligned} \tag{42}$$

where G is a matrix, with dimensions prescribed by the two ports.

6.1.3 An intuitive example: the mass-spring system

In an attempt to consolidate these new concepts, we present the simple mass-spring system in port-Hamiltonian language, using the example given in [31].

We consider a mass m to be moving, without friction, under the influence of a linear spring with spring constant k . If we take the rest length of the spring to be x_0 , then the trajectory of this system is defined by the second-order differential equation

$$m\ddot{x} = -k(x - x_0). \tag{43}$$

If we instead regard this example as the interconnection of two energy-storing subsystems – the *mass* which stores kinetic energy, and the *spring* which stores potential energy – then we can represent the system by Fig. 25. For an overview of the storage elements for different physical domains, we refer the reader to Section 9.3.

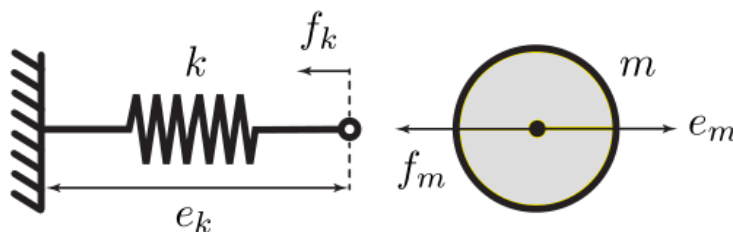


Figure 25: Interconnection of mass and spring subsystems.

The potential energy of the linear spring is determined by the extension $q = x - x_0$; using Hooke's law we find that the energy is equal to $\frac{1}{2}kq^2$. If we take the velocity and force at the the *end* of the spring, denoting them by $-f_k$, and e_k respectively, then we find the system equations

$$\begin{aligned} \dot{q} &= -f_k, \\ e_k &= \frac{d}{dq} \left(\frac{1}{2}kq^2 \right). \end{aligned} \tag{44}$$

Similarly, we can take the kinetic energy of the mass to be given by $\frac{1}{2m}p^2$, with p being the mass momentum, such that

$$\begin{aligned} \dot{p} &= -f_m, \\ e_m &= \frac{d}{dp} \left(\frac{1}{2m}p^2 \right). \end{aligned} \tag{45}$$

It is easy to see that $-f_m$ defines the force on the mass, while e_m denotes its velocity. Just as we assumed in the previous sections that the solid and the fluid would share motion properties along

the boundary, we can safely assume that the subsystems are linked such that the velocities are equal, and the forces are negative. Therefore, we find the coupling equations

$$\begin{aligned} -f_k &= e_m, \\ f_m &= e_k. \end{aligned} \tag{46}$$

Finally, if we take the Hamiltonian $H(q, p)$ to define the total energy of the system, then we find that the complete system can be described by

$$\begin{bmatrix} \dot{q} \\ \dot{p} \end{bmatrix} = \begin{bmatrix} 0 & 1 \\ -1 & 0 \end{bmatrix} \begin{bmatrix} \frac{\partial H}{\partial q}(q, p) \\ \frac{\partial H}{\partial p}(q, p) \end{bmatrix}, \quad H(q, p) = \frac{1}{2}kq^2 + \frac{1}{2m}p^2. \tag{47}$$

This example shows how the *flows* and the *efforts* work within the physics of the problem, but also how the skew-symmetric matrix represents the Dirac structure governing the exchange of energy in the system, given by Eq. (46). It should be clear to the reader that this formulation would maintain the same structure were we to look at a three-dimensional system. In such a case, we would replace the arguments (q, p) by (\mathbf{q}, \mathbf{p}) , and modify the coupling matrix to be $\begin{bmatrix} 0 & I_3 \\ -I_3 & 0 \end{bmatrix}$, where I_3 is the 3×3 identity matrix.

Before we progress, it is worthwhile to discuss what the flow and effort of a system actually represents. The *flow* of a physical domain represents the *time rate of change* of the storage variable: in the previous model, the storage variable of the spring was the *displacement*, so the flow was the *velocity*; while the storage state for the mass was the *momentum*, meaning that the flow was a *force*. For readers who have studied dynamical systems, the notion used here is similar to the definition of a *flow* describing the trajectory of a system over the governing state space manifold. In the port-Hamiltonian framework, we take the flow to be the tangential direction at every point along the state space trajectory. Similarly, the *efforts* of each domain are the partial derivatives of the Hamiltonian, with respect to the necessary energy variable, i.e., we see how much the total energy of the system is changing due to a specific parameter.

Thus, for a general energy-storing element \mathcal{S} , with storage variable x , we define the flow and effort to be²⁴

$$f_S = -\dot{x} \quad \text{and} \quad e_S = \frac{\partial H}{\partial x}(x). \tag{48}$$

This formulation is also where the term *power variables* comes from, as the time rate of change of the (Hamiltonian) energy, i.e., the *power*, is given by

$$\frac{dH}{dt} = \frac{\partial^T H}{\partial x}(x)\dot{x} = -e_S^T f_S, \tag{49}$$

with the negative term denoting the energy flow *from* \mathcal{S} into the Dirac structure \mathcal{D} .

6.2 Description of the model

With this brief overview of port-Hamiltonian systems, we can now make an attempt to describe the solid-fluid coupled model in this new language. Fig. 26 shows how the model can be divided into separate physical domains, with the shared boundary acting as a bridge between the two.

²⁴Due to the new notation \mathcal{S} denoting a general, *grouped* storage element, from now on we will use the subscripts m and f to denote the *mass* and the *fluid*.

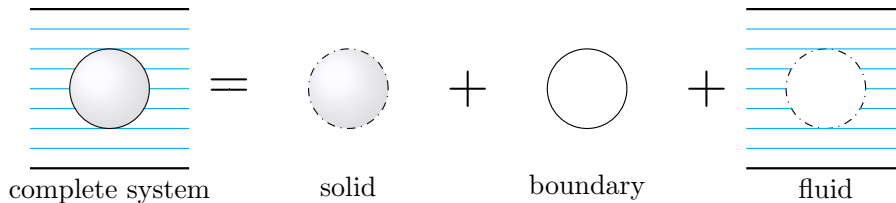


Figure 26: A port-based description of the FSI model.

What we would like to construct is a form similar to what we derived in Section 6.1.3, whereby the necessary equations that emerge from the Hamiltonian formulation specify the port-Hamiltonian structure. However, the fundamental difference here is that we are not representing a finite degree-of-freedom, mechanical system any more, but instead we may need to use an infinite degree-of-freedom representation for the fluid domain.

6.2.1 Governing equations

Taking a similar starting point to Section 6.1.3, we can understand the system as the union of two energy-storing domains, but this time they *both* store kinetic energy²⁵. This is not a problem for the solid, which we have assumed to have uniform density and a symmetric centre of mass. In fact, we get exactly the same form as Eq. (45), only now we have three dimensions to work with. Thus, the kinetic energy of the solid is given by

$$\mathcal{T}_s = \frac{1}{2m} |\mathbf{p}|^2, \quad (50)$$

where we use a vector quantity \mathbf{p} to represent the momentum. If we then take the fluid domain to be denoted by Ω , we will also find that the kinetic energy of the fluid is

$$\mathcal{T}_f = \int_{\Omega} \frac{1}{2} \rho |\mathbf{u}|^2 d\Omega, \quad (51)$$

where ρ is the fluid density, and \mathbf{u} is the (pointwise) fluid velocity vector, defined over the entire fluid domain. If we sum the two energies, then we find the total-energy Hamiltonian

$$H(\mathbf{p}, \mathbf{u}) = \frac{1}{2m} |\mathbf{p}|^2 + \int_{\Omega} \frac{1}{2} \rho |\mathbf{u}|^2 d\Omega. \quad (52)$$

Although we have followed similar steps to Section 6.1.3, we have a slightly different Hamiltonian equation, due to the fact that the fluid domain is not a finite degree-of-freedom subsystem. In general, this is referred to as a *distributed parameter* system. To be able to manipulate the integral term to find Hamiltonian equations, we must explore the realm of functional analysis, looking at Hamiltonian fluid dynamics in an infinite-dimensional setting. We refer to [16, 17, 22] for an in-depth look at Hamiltonian fluid dynamics, but for this thesis the following overview will suffice²⁶.

A *functional* is a real-valued function on a vector space \mathcal{V} , usually of functions, i.e., it is a map that takes functions as an input, and outputs real numbers. In our case, if we were looking at a

²⁵In this simple case, we assume that the fluid is incompressible, and the solid is neutrally buoyant, such that we can neglect the inclusion of potential energy.

²⁶The field of Hamiltonian fluid dynamics is one which is not easily accessible, especially from an undergraduate viewpoint. However, every effort has been made to simplify the results found such that they can be understood by the reader.

one-dimensional fluid, we would have the functional

$$T[u] = \frac{1}{2} \int_a^b \rho u^2 dx, \quad (53)$$

where the input is the velocity function $u(x)$. If we were to input different velocity functions into $T[u]$, then we would retrieve different scalar values, corresponding to the kinetic energy of the one-dimensional fluid domain. To explain the nuances of functionals would not be helpful to this study, but some important techniques should be made clear, to be able to understand how to deal with infinite-dimension Hamiltonians.

We will need to look at *functional derivatives*, a generalization of the usual derivative, whereby we differentiate the functional with respect to a function such that

$$\frac{\delta T[u(x)]}{\delta u(x_0)} = \lim_{\epsilon \rightarrow 0} \frac{T[u(x) - \epsilon \delta(x - x_0)] - T[u(x)]}{\epsilon}. \quad (54)$$

Here, $\epsilon \delta(x - x_0)$ represents the *variation* $\delta u(x)$, with $\delta(x - x_0)$ being the *Dirac delta function*, and ϵ being a small number. This would then find that the functional derivative of Eq. (53) would be

$$\frac{\delta T}{\delta u} = \rho u. \quad (55)$$

To show that the idea can be extended to multi-function functionals, and higher-dimensional domains, if we took the functional

$$T[\rho, \mathbf{u}] = \frac{1}{2} \int_{\Omega} \rho |\mathbf{u}|^2 d^3x \quad (56)$$

then the functional derivatives would be

$$\frac{\delta T}{\delta \rho} = \frac{1}{2} |\mathbf{u}|^2, \quad (57)$$

$$\frac{\delta T}{\delta u_i} = \rho u_i, \quad \text{for } i = 1, 2, 3. \quad (58)$$

It is useful to note that if we remove the above dependence on ρ , then we are left with a solution that comes directly from Eq. (51), only now we have a functional derivative, rather than just a partial derivative, to denote the *effort*. The missing piece of the puzzle would therefore seem to be whether to use a *flow* of the form $\dot{u}_i = a_i$. However, an important question remains; *Should this be used in an infinite-dimensional form, or a finite-dimensional form?*

As a slight aside, we refer to the work by Morrison [16], which serves as a general overview of the whole study of Hamiltonian fluid dynamics, in which there are discussions on functional calculus, canonical and non-canonical Hamiltonian formulations, Poisson bracket notation, among many other things. It would not serve the purpose of this study to re-write everything that is mentioned, but it could certainly be enlightening to discuss the evolution of the *canonical* Hamiltonian form, with a paraphrased derivation given in Section 9.4 for keen readers. For those who do not have the need for a full derivation, we shall instead just progress with the results.

The canonical form of an ideal fluid, this time including the potential energy, finds that the Hamiltonian is described by

$$H[\pi, \mathbf{q}] = \int_{\Omega} \left(\frac{\pi^2}{2\rho_0} + \rho_0 U \right) d^3a, \quad (59)$$

where

- π is the *canonical momentum density*, $\pi_i = \rho_0 \dot{q}_i$
- ρ_0 represents the *initial mass density configuration* over the domain Ω
- $\rho_0 U$ is the initial *energy per unit volume* of the fluid

The reason for the differential being of the form d^3a is due to the fact that this approach takes a Lagrangian framework of fluid dynamics, rather than an Eulerian one. This uses the notion that each fluid element has an initial ‘label’, a , meaning that it can be tracked throughout the domain over time. However, we still integrate the fluid over a domain $\Omega \subset \mathbb{R}^3$.

We note a similarity between Eq. (59) and Eq. (52), as the definition of π suggests that $\pi_i = \rho_0 u_i$ in our original notation. However, we will keep Morrison’s notation such that the reader is able follow the original arguments in [16], if necessary, without having to translate between the two.

From Eq. (59), it is then found that the infinite-dimensional Hamilton equations can be written as

$$\dot{\pi}_i = -\frac{\delta H}{\delta q_i}, \quad \dot{q}_i = \frac{\delta H}{\delta \pi_i} \quad \text{for } i = 1, 2, 3. \quad (60)$$

Finally, these forms are condensed by means of a *Poisson bracket*

$$\{F, G\} = \int \left[\frac{\delta F}{\delta q} \cdot \frac{\delta G}{\delta \pi} - \frac{\delta G}{\delta q} \cdot \frac{\delta F}{\delta \pi} \right] d^3a, \quad (61)$$

such that Eqs. (60) can be written as

$$\dot{\pi}_i = \{\pi_i, H\}, \quad \dot{q}_i = \{q_i, H\}. \quad (62)$$

Although we do not use this notation in this thesis, it is again useful for readers who wish to pursue a further understanding of Hamiltonian fluid dynamics. We will now discuss the difficulties in trying to marry the two types of Hamiltonians together, to form a port-Hamiltonian system.

6.2.2 Attempting to couple the equations

Let us write the three energy formulae as separate forms, before we try to merge any of them together. Firstly, we have the kinetic energy of the solid, which we already know to be

$$H_1(\mathbf{p}) = \frac{1}{2m} |\mathbf{p}|^2. \quad (63)$$

Secondly, we have two possible expressions to use for the energy of the fluid; the ideal incompressible version, without potential,

$$H_2[\mathbf{u}] = \int_{\Omega} \frac{1}{2} \rho |\mathbf{u}|^2 d\Omega; \quad (64)$$

and the general *canonical* form, with potential,

$$H_3[\pi, \mathbf{q}] = \int_D \left(\frac{\pi^2}{2\rho_0} + \rho_0 U \right) d^3a. \quad (65)$$

The kinetic energy from the solid must obviously be included, yet it must be paired up with not a function, but a functional. This means that we cannot have the standard *flow* and *effort* expressions, because we will need a partial derivative in one case, and a functional derivative for the other.

Without regarding the specificities of the mathematics, it appears as though there could be a link

between H_1 and H_3 , as they have the shared property of being defined by the *momentum* of the model. As we have seen, for the equations of the solid, we will find

$$\text{mass} = \begin{cases} \dot{\mathbf{p}} & = -f_m, \\ e_m & = \frac{d}{d\mathbf{p}} \left(\frac{1}{2m} |\mathbf{p}|^2 \right), \end{cases} \quad (66)$$

such that we have an expected (f_m, e_m) port, with respect to this component. In the fluid model, we have the momentum density $\pi = \rho_0 \dot{\mathbf{q}}$, from which we could find a ‘force density’, $\mathcal{F} = \dot{\pi} = \rho_0 \ddot{\mathbf{q}}$. By integrating this term over the entire fluid domain, we would obtain a representation of the net fluid force, $\mathbf{F} = \int_{\Omega} \mathcal{F} d\Omega$.

However, we do not need the net force over the *entire* domain, so with the coupling assumptions we could instead impose the condition that there was a force balance over the surface, such that

$$-f_m = \dot{\mathbf{p}} = -\tilde{\mathbf{F}}, \quad (67)$$

where $\tilde{\mathbf{F}} = \int_{\Gamma} \mathcal{F} d\Gamma$ is instead the integrated force density over the boundary surface.

Matching the velocity condition is a little different, as we have a more restrictive constraint at the boundary. With the force balance, we could assume that the total net force of the fluid was opposed by the force of the mote, and so this meant that (pointwise) the fluid force could be acting in *any* direction, so long as the entire integral balanced out. Regarding the velocity of the fluid, the no-slip condition means that each fluid element must have the same velocity as the point of the mote surface that it is touching. The difference with this notion is that the mote is a solid body, and so we make the continuum assumption that all solid particles travel with the same velocity as one another. This therefore means that each *fluid* particle at the surface must necessarily be travelling with the same velocity.

This could possibly be a useful approach though, as it necessarily reduces the expected velocity function acting over the surface, to just a constant velocity, i.e.,

$$\dot{q}_i = v_i, \quad \text{for } i = 1, 2, 3, \quad (68)$$

where v_i is the i^{th} component of the mote velocity vector. Thus, the difficulty of incorporating the infinite-dimensional velocity function is removed, as the no-slip condition guarantees a constant value over the mote surface at any given time instant.

Therefore, our assumptions about the fluid behaviour at the mote surface suggest that we have three integral conditions,

$$-f_m^i = \dot{p}_i = - \int_{\Gamma} \mathcal{F}_i d\Gamma \quad \text{for } i = 1, 2, 3, \quad (69)$$

and three constant conditions,

$$e_m^i = \frac{d}{dp_i} \left(\frac{1}{2m} |\mathbf{p}|^2 \right) = \dot{q}_i \quad \text{for } i = 1, 2, 3. \quad (70)$$

It should hopefully be clear to the reader that the velocity boundary condition acts as a restriction on the functional space from which we are able to draw velocity functions²⁷. This formulation is

²⁷Observant readers may possibly be thinking: *But what if we take a mote with angular velocity, such that the solid continuum assumption does not hold?* In response, we say that if we add in a rotational component into the system, then we will necessarily have an *additional* storage element, meaning that the kinetic energy of the mote would need to be amended to include the *rotational* kinetic energy $T_r = \frac{1}{2} I \omega^2$. This obviously makes the system more complex, so it was ignored for this part of the thesis, even though rotational effects *were* included in the computation section.

useful to see that we can certainly share information between the finite-dimensional and infinite-dimensional sub-systems, but it does not necessarily bridge the gap in the analytical description.

The difficulty lies in finding an operator that would connect the partial and functional derivatives from the two domains, maintaining the surface relationship

$$\begin{aligned} \dot{p}_i &= - \int_{\Gamma} \frac{\delta H_3}{\delta q_i} d\Gamma, \\ \frac{dH_1}{dp_i} &= \dot{q}_i \Big|_{\Gamma}. \end{aligned} \tag{71}$$

This at least seems to have *some* semblance of the port-Hamiltonian form of Section 6.1.3.

From the canonical Hamiltonian description of a fluid, this also means that we could rewrite these equations in terms of the density, to *nearly* find a transformer form

$$\begin{aligned} \dot{p}_i &= - \int_{\Gamma} \dot{\pi}_i d\Gamma, \\ \frac{dH_1}{dp_i} &= \frac{\delta H_3}{\delta \pi_i} \Big|_{\Gamma}. \end{aligned} \tag{72}$$

Unfortunately, the usefulness of these equations was not discovered, as we were unable to make any more progress than this point in the time available.

6.2.3 A different coupling perspective

An alternative approach is to make a certain assumption about the formulation of the Hamiltonian energy equation, to then see how we could progress with respect to a finding the necessary Dirac structure to make the port-Hamiltonian system. Looking at Section 9.3, we note that in our simplified model, we are looking at the *kinetic translation* domain, and the *kinetic hydraulic* domain, ignoring any potential energy. The solid behaviour is governed in terms of the storage state x_m , which happens to be the momentum of the solid. This agrees with what we have previously given as the energy in Eq. (63).

The fluid is therefore governed by the storage state x_f , which in this physical domain is the *flow tube momentum*, which we denote here by η . The flow and effort are then defined as the *pressure* and *volume flow*, respectively. Let us now forgo the construction of the Hamiltonian energy equation and just assume that it does exist, denoting it by $H_f(\eta)$. Therefore, the energy of the entire system is given by

$$H(\mathbf{p}, \eta) = \frac{1}{2m} |\mathbf{p}|^2 + H_f(\eta). \tag{73}$$

With this in mind, we expect the flow and effort should satisfy the canonical equations (48), such that we find that the kinetic translation domain is described by

$$\text{mass} = \begin{cases} \dot{\mathbf{p}} = -f_m, \\ e_m = \frac{\partial H}{\partial \mathbf{p}} = \frac{\partial}{\partial \mathbf{p}} \left(\frac{1}{2m} |\mathbf{p}|^2 \right) = \mathbf{v}, \end{cases} \tag{74}$$

and the hydraulic domain is governed by

$$\text{fluid} = \begin{cases} \dot{\eta} = -f_f, \\ e_f = \frac{\partial H}{\partial \eta} = \dot{V}, \end{cases} \tag{75}$$

where η denotes the *pressure*, and \dot{V} is the *volume flow*.

Let us now look at the physical interpretations of these equations. Eqs. (74) show us that the flow of the mechanical domain is a *force*, while the effort is a *velocity*. Again, these are useful because we have assumed constraints on the force and velocity of the solid *and* fluid at the shared boundary, yet the hydraulic domain is not described by these terms. This means that we require an operator that acts between the two domains for the physical dimensions to agree, shown by Fig. 27, mirroring the coupling of the solid and the fluid.

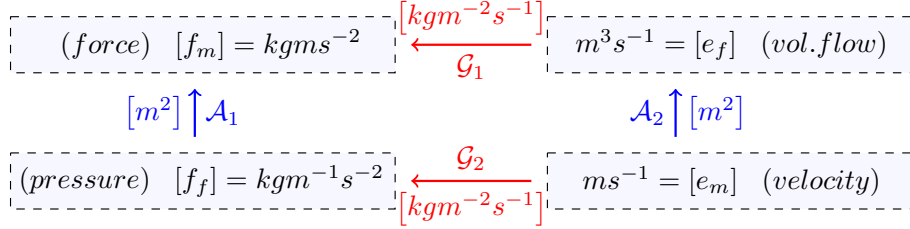


Figure 27: Dimension-matching pairings of the solid-fluid equations via an ‘area’ operator, and an ‘area-density-per-second’ operator.

Fig. 27 shows that there are two different ways in which we can couple the domains, either in the form

$$\begin{aligned} f_m &= -\mathcal{A}_1 f_f, \\ e_f &= \mathcal{A}_2 e_m, \end{aligned} \quad (76)$$

or alternatively, using

$$\begin{aligned} f_m &= -\mathcal{G}_1 e_f, \\ f_f &= \mathcal{G}_2 e_m, \end{aligned} \quad (77)$$

where \mathcal{A}_i and \mathcal{G}_i are general operators, for $i \in \{1, 2\}$, which pair the necessary physical dimensions. Note that we write these forms in such a way that the *force* variable, f_m , is the opposite to what it is paired with, corresponding to Newton’s Third Law, while the *velocity* variable, e_m , has equations which are in positive agreement, representing the no-slip surface condition.

There are clear similarities between Eqs. (76) and (77), and Eqs. (41) and (42), but we must look a little further to understand which form we should try to use. Looking at Eqs. (76), due to the fact that we are analysing at the system so generally, we do not entirely know what the relationship between \mathcal{A}_1 and \mathcal{A}_2 will be. It would be somewhat useful if we could say that there was a symmetric relationship between the two operators, i.e., $\mathcal{A}_2 = \mathcal{A}_1^*$, as then we would be able to give the domain coupling in terms of general *transformer* equations. Similarly, it would be useful for Eqs. (77) if we found that $\mathcal{G}_2 = \mathcal{G}_1^*$, to find a general *gyrator* coupling of the FSI system. It is important to know that we do not specifically *need* either of these forms, but having a symmetric relationship such as this allows for greater manipulation of future results.

From this point onwards, we shall work with only the coupling scheme described by Eqs. (76), for two reasons, the first being that all following argumentation can be applied to Eqs. (77), and so investigating both forms would be redundant. Secondly, the ‘area’ operator seems far more intuitive to use, with respect to coupling over the surface of the mote, rather than trying to describe exactly what the ‘area-density-per-second’ operator actually represents.

Given that we have found these equations from the generalised Hamiltonian (73), we understandably cannot work deeply with the operators \mathcal{A}_1 and \mathcal{A}_2 in their current form, as we know nothing about them. However, it may be useful to again *assume* that we have the necessary symmetric relationship, to then explore what we can say about the system if this were the case, i.e., we have the equations²⁸

$$\begin{aligned} f_m &= -\mathcal{A}f_f, \\ e_f &= \mathcal{A}^*e_m. \end{aligned} \tag{78}$$

This assumption can be explained in three steps. Firstly, given that we are looking for a global relationship between the two domains, it is not completely unlikely that the same operator governs the entire relationship between the mote and the fluid, i.e., the relationship between *force* and *pressure* is inherently linked to the relationship between *volume flow* and *velocity*. Secondly, as mentioned before, the satisfaction of Newton’s Third Law, and the surface no-slip condition ensure that one coupling equation is *negative*, while the other is *positive*. Finally, we recall that the coupled variables must have (pairwise) equal dimensions, i.e., the ‘size’ of f_m and e_m are equal, and the same holds for f_f and e_f . From the assumption of the global operator \mathcal{A} , this means that we require the *adjoint* operator \mathcal{A}^* to govern the second equation.

If we were to look at this relationship in a finite-dimensional framework, then we would instead have the matrix form

$$\begin{aligned} f_m &= -\mathbf{A}f_f, \\ e_f &= \mathbf{A}^T e_m, \end{aligned} \tag{79}$$

whereby the dimensions of \mathbf{A} are specified by the port variables. Even though the details of this operator are not completely defined, we will utilise this matrix form in Section 7.2, when creating the the crossover between the two disciplines discussed in this thesis.

²⁸The reader may question why we make such assumptions, without knowing the specific form of the Hamiltonian function, nor the coupling operator. A more general coupling operator may be worthwhile to explore, but interesting results could not be found in the limited time remaining. To satisfy the reader, in Section 9.5 we include all following work without the symmetric assumption, to show the difference in simplicity and clarity.

7 A Numerical Port-Hamiltonian Scheme

To end this study, we wish to try and form a bridge between the two disciplines of Computational and Numerical Mathematics, and Port-Hamiltonian Systems. We hope to provide an initial look into how the concepts could be connected, drawing on the power balance of port-Hamiltonian systems, while acknowledging the inherent errors of numerical models. This chapter builds on ideas from the texts already mentioned in previous chapters, as well as the paper by Talasila et al. [26], which looks specifically at *discretized* port-Hamiltonian systems.

7.1 Description of the numerical model

Let us make an assumption from the previous section that we are in possession of a port-Hamiltonian system describing the coupled solid-fluid dynamics, such that we have the two domains governed by a Dirac structure, as shown in Fig. 28.

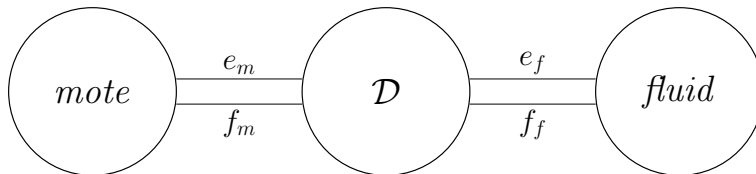


Figure 28: An idealised, solid-fluid port-Hamiltonian system.

In this idealised model, we know that there should be a power balance, such that the energy-routing element is indeed a Dirac structure. However, if we look back to the first section of this paper, the numerical model is predicated on *ComFLOW* running an iteratively coupled scheme, calculating the forces and accelerations acting at the solid-fluid boundary. This means that at each step in the program, the fundamental values of *force*, *acceleration*, *velocity*, and *position* are not explicitly known, but instead must be computed to an accurate enough degree. This requirement for accuracy allows the model to maintain its stability, but in terms of the power balance at each iteration, there will understandably be a non-zero sum, due to the inexact nature of the approximating values.

We will now go over some results from [26], covering the construction of discrete port-Hamiltonian systems, culminating in a discretized example of the mass-spring system. To end this section, we will attempt to apply a similar viewpoint to describe iteratively coupled computational methods.

By constructing the discretized model, it would be useful to necessarily work in the space \mathbb{R}^n , rather than be working in function spaces, hopefully making the problem simpler as we do not have the difficulty of trying to marry a finite-dimensional space with an infinite-dimensional one. That said, we will follow the convention used in [26], whereby it is mentioned that due to the discretization process we are no longer working over the field \mathbb{R} , but instead we utilise the *quasi-ring* of floating-point numbers, denoted \mathbb{F} . This detail is necessary due to the finite accuracy of machine simulations, meaning that our space of working is therefore the floating point lattice \mathbb{F}^n .

Similar to how the Hamiltonian was defined on the state space \mathcal{X} , such that $H : \mathcal{X} \rightarrow \mathbb{R}$, we will instead be defining the discretized Hamiltonian as $H : \mathbb{F}^n \rightarrow \mathbb{F}$. We do not change the notation for the Hamiltonian, as the basic concept is exactly the same as before. However, we now need to define the discretized equivalent of tangent vectors, such that we can define a discretized flow, by taking the tangent space to be

$$T_p\mathbb{F}^n := \{(p, q) \in \mathbb{F}^n \times \mathbb{F}^n\}, \quad (80)$$

such that a *discrete vector* at $p \in \mathbb{F}^n$ is described by the pair (p, q) , i.e., an initial point p and a translation vector q . It should be noted that there are multiple representations for a discrete vector, dependent on the type of integration technique being used in the numerical model, however these will not be looked at in this thesis, so keen readers are advised to find more in [26].

If we recall that the trajectory of the Hamiltonian over the state space represents the Hamiltonian function as the system progresses through time, then we are also able to use a *discrete vector field* to represent the same behaviour. We can define a discrete vector field as a mapping X which assigns each point on the lattice \mathbb{F}^n a specific vector q , such that $X(p) = (p, q)$. Much like the *flow vector* on the smooth manifold is the instantaneous time rate of change of the energy variable, such that we create a smooth energy trajectory, we can also describe the same flow in a discretized vector field by the sequence of points p_0, p_1, p_2, \dots in \mathbb{F}^n . This succession of points then discretizes the *smooth* flow trajectory of the original system.

The concept of a Dirac structure follows the same formulation as in previous cases, only this time we are taking the space of power variables for be $\mathbb{F}^n \times \mathbb{F}^n$. We still denote the ports by (f, e) , such that we can define the Dirac structure to be the subspace $\mathcal{D} \subset \mathbb{F}^n \times \mathbb{F}^n$, such that $\langle e | f \rangle = 0$ for all pairs $(f, e) \in \mathcal{D}$. Talasila et al. discuss the possible representations of discrete Dirac structures, as well as the interconnection between multiple Dirac structures, however they will not be included in this study, as they are beyond the scope of what is needed. The final points to be discussed here regard the discrete representation of the Hamilton equations.

We assume that everything up to this point is well-posed, and so for a system with n energy-storing elements, denoted z_1, \dots, z_n , acting as coordinates for a n -dimensional *discrete* manifold \mathcal{Z} , then the discrete Hamiltonian is the total energy function $H : \mathcal{Z} \rightarrow \mathbb{F}$. As we are working in the discrete setting, we do not have the tools necessary to represent an exact derivative of the energy variable, so instead we use the ratio $\Delta z / \Delta t$. Similarly, because we cannot use *exact* spatial derivatives, with respect to the energy-storing elements, then we replace $\frac{\partial H}{\partial z}$ by the discrete notation $\partial_z H(z)$, to keep with what is used in [26].

If we recall the power balance given by Eq. (49), then Talasila et al. showed that the discrete formulation of this will instead be

$$-\partial_z H(z) \cdot \frac{\Delta z}{\Delta t} + e^T f = 0. \quad (81)$$

It would be useful if we could include the ratio $\Delta H / \Delta t$ into this formula, but unfortunately the chain rule does not hold in the discrete framework, so we cannot simply replace

$$\Delta H / \Delta t = \partial_z H(z) \cdot \Delta z / \Delta t. \quad (82)$$

Instead, what we are able to do is to incorporate an additional power term \tilde{H} , which is an artefact of the discretization process, such that

$$\frac{\Delta H}{\Delta t} = -\partial_z H(z) \cdot \frac{\Delta z}{\Delta t} + e^T f - \tilde{H} = 0. \quad (83)$$

Fig. 29 gives a representation of the additional port needed to maintain the power balance, such that as the discretization becomes finer, the value of \tilde{H} tends to zero²⁹.

²⁹In this study we take an alternate approach, such that we want \tilde{H} to tend to zero as the *coupled iterations* become more accurate, regardless of the discretization we choose for the model.

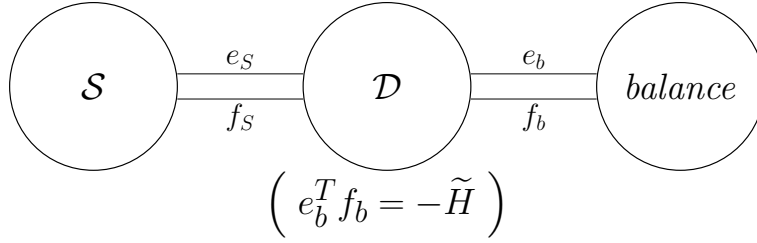


Figure 29: The discrete Dirac structure, preserved by the additional balance port.

Using the mass-spring example from Section 6.1.3, we would find that we could discretize the system equations

$$\begin{bmatrix} \dot{q} \\ \dot{p} \end{bmatrix} = \begin{bmatrix} 0 & 1 \\ -1 & 0 \end{bmatrix} \begin{bmatrix} \frac{\partial H}{\partial q}(q, p) \\ \frac{\partial H}{\partial p}(q, p) \end{bmatrix}, \quad (84)$$

into the form

$$\begin{aligned} \frac{\Delta q}{\Delta t} &= \partial_p H(q, p), \\ \frac{\Delta p}{\Delta t} &= -\partial_q H(q, p). \end{aligned} \quad (85)$$

Note that for both systems we still use the Hamiltonian $H(q, p) = \frac{1}{2}kq^2 + \frac{1}{2m}p^2$, however for the smooth system we take values over the field \mathbb{R} , while for the discretized system we take values over \mathbb{F} .

7.2 Introducing an iterative scheme

Assuming that the formulation in Section 6.2.3 is well-defined, we can take an initial step into the discretization of iteratively coupled numerical methods, which was not covered in the work by Talasila et al. In our numerical model, we know that there is a need for an iterative scheme to be computed, such that this process converges to within a certain accuracy. This type of formulation would appear to be described by the discretized port-Hamiltonian system, noting that the imbalance between the computed forces and velocities would create a non-zero power summation. Therefore, as described in the previous section, we could include an additional port into the model such that the power-balance is restored, shown by Fig. 30.

This inclusion is supported by the work in [26], but we wish to find a specific representation of the *balance port* (f_b, e_b) . It is discussed in the previously mentioned works [23, 26, 30, 31] that closely related to the definition of *power* is the canonically defined bilinear form over the space of power variables, $\mathcal{F} \times \mathcal{E}$, such that

$$\langle\langle (f_X, e_X), (f_Y, e_Y) \rangle\rangle := \langle e_X, f_Y \rangle + \langle e_Y, f_X \rangle \quad (86)$$

for all $(f_X, e_X), (f_Y, e_Y) \in \mathcal{F} \times \mathcal{E}$.

If we assume that there indeed exists a power imbalance between the solid and fluid ports, i.e., between $e_m^T f_m$ and $e_f^T f_f$, then we will need the additional port such that

$$e_m^T f_m + e_f^T f_f + e_b^T f_b = 0. \quad (87)$$

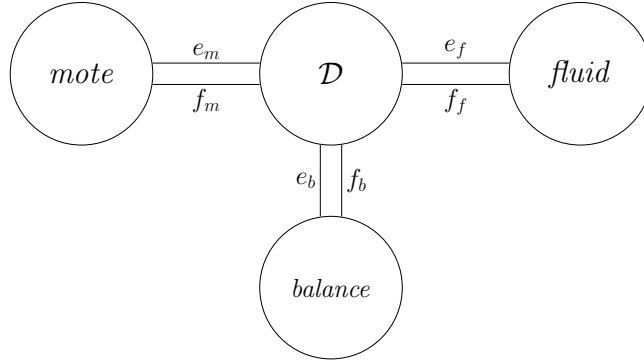


Figure 30: The discrete port-Hamiltonian FSI system, preserved by the additional balance port.

Rearranging this, we would find

$$\begin{aligned} e_b^T f_b &= -e_m^T f_m - e_f^T f_f, \\ &= -\left(\langle e_m, f_m \rangle + \langle e_f, f_f \rangle \right). \end{aligned} \quad (88)$$

Although this seems to have a form such that we could state $e_b^T f_b = -\langle\langle (f_f, e_m), (f_m, e_f) \rangle\rangle$, we note that this does not necessarily make sense. This is due to the fact that although the inner products are well defined, we may not find that f_f and f_m are taken from the same space \mathcal{F} , given that we have the coupling condition $f_m = -\mathbf{A}f_f$, meaning that the canonical bilinear form may not be well-defined. However, we still find a condition on the balance port such that it must be equal to the negative sum of the other duality products, for the power balance to be satisfied, so we must necessarily look for the specific port variables that match this value.

Unfortunately, there is no guarantee that we will always be able to find a pair of port variables which guarantee this balance, even if we work over \mathbb{F} . This is because Eq. (88) is akin to stating that we can always find steady, coupled solutions across any boundary, which is not necessarily true for systems which are highly non-linear. For linear, steady-state systems, there may well be port variables which maintain the power balance, but for general systems this is not the case.

In light of this, an alternate way to look at the problem would be to assume that due to the inherent imbalance at the numerical level, basing the following on Eqs. (79), we have that the discrete port-Hamiltonian equations are actually of the form

$$\begin{aligned} f_m &= -\mathbf{A}f_f + \gamma, \\ e_f &= \mathbf{A}^T e_m + \psi, \end{aligned} \quad (89)$$

where γ and ψ represent non-exact agreement in the numerical Hamiltonian equations³⁰, and we use the matrix form \mathbf{A} because we are working in a discrete space. The reader may think of the matrix \mathbf{A} as being the numerical coupling between the discretized mote and the discretized fluid, which may or may not be square, depending on the discretizations of the two domains.

From this point, let us again include an additional port to conserve the power balance, such that

³⁰Note that γ represents an error of the same dimension as f_m , while ψ represents an error of the same dimension as e_f . Thus, they may not necessarily be of the same dimension, assuming $\gamma \in \mathbb{F}^\alpha$, and $\psi \in \mathbb{F}^\beta$.

Eq. (87) is satisfied. Using Eqs. (89), we therefore find

$$\begin{aligned}
e_b^T f_b &= -\left(e_m^T f_m + e_f^T f_f\right), \\
&= -\left(e_m^T (\mathbf{A} f_f + \gamma) + (-\mathbf{A}^T e_m + \psi)^T f_f\right), \\
&= -e_m^T \mathbf{A} f_f - e_m^T \gamma + e_m^T \mathbf{A} f_f - \psi^T f_f, \\
&= -(e_m^T \gamma + \psi^T f_f), \\
&= -(\langle e_m, \gamma \rangle + \langle \psi, f_f \rangle).
\end{aligned} \tag{90}$$

Thus, it would be useful if we could define the additional pair $(f_b, e_b) \in (\mathbb{F}^\alpha \times \mathbb{F}^\beta) \times (\mathbb{F}^\alpha \times \mathbb{F}^\beta)$ to be of the form

$$-f_b = \begin{bmatrix} \gamma \\ \cdots \\ \psi \end{bmatrix}, \quad \text{and} \quad e_b = \begin{bmatrix} e_m \\ \cdots \\ f_f \end{bmatrix}. \tag{91}$$

By choosing these as the balancing flow and effort, then not only would the Dirac structure be maintained for the discretized framework, but it also has the added effect that as the numerical imbalances are reduced, i.e., if $\gamma \rightarrow \mathbf{0}$ and $\psi \rightarrow \mathbf{0}$, then the additional power *also* tends to zero. It is worth noting that these two vectors don't have any *real* physical meaning within the model, but are merely place-holders used to maintain the Dirac structure power balance.

With this in mind, we can now look at what happens when we have coupled iterations of a computational model that must converge to within a required tolerance. We will use the previous models as an example, whereby *ComFLOW* must iteratively compute the forces and motions of the mote and the fluid at each time step, until they are within a desired accuracy from one another. We can describe this discretized port-Hamiltonian system using Fig. 31, where we use the **old** fluid to find the **new** solid, which then finds the **NEW** fluid, to then restart the cycle.

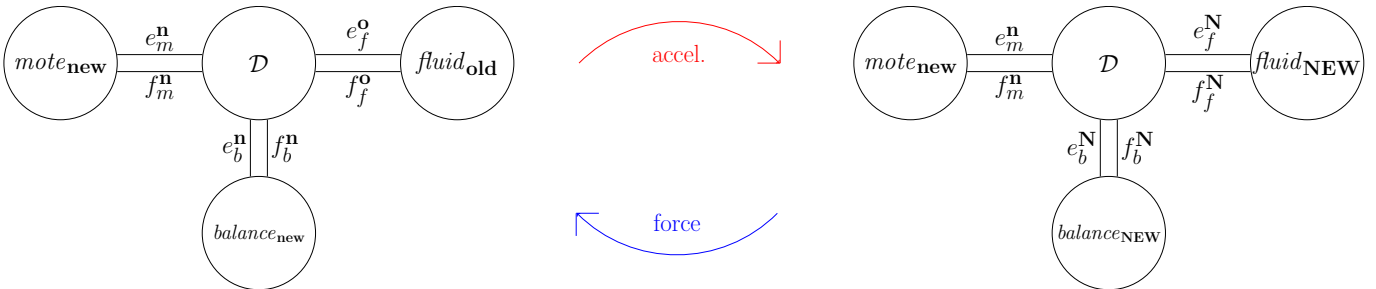


Figure 31: A general depiction of the *iteratively coupled* port-Hamiltonian scheme. Note that the balance port is updated with *each* step, so we have *two* different balance pairs in a single cycle, corresponding to the lower case and upper case superscripts.

In this case, we have the same requirements as just discussed, only now we have the added *iterative constraint*, meaning that we require that the additional product, $e_b^T f_b$, tends to zero. There is a subtle difference between this requirement and what is discussed in Talasila et al., in which they state that the additional energy \tilde{H} will tend to zero if the spatial discretization becomes more accurate. In this new framework, we do not enforce a greater accuracy of the mesh, but rather we need the

iterative procedure to converge, meaning that our numerical error tends to zero.

To explore this scheme further, we will employ the use of multiple graphical representations, to stress what variables are being updated during each iteration. In the iterative coupling process, via Eqs. (79), we use the pressure to find the force, and the velocity to find the volume flow; Fig. 32 shows this relationship. This figure may not be immediately clear, so we will explain each component part to build up to the whole scheme.

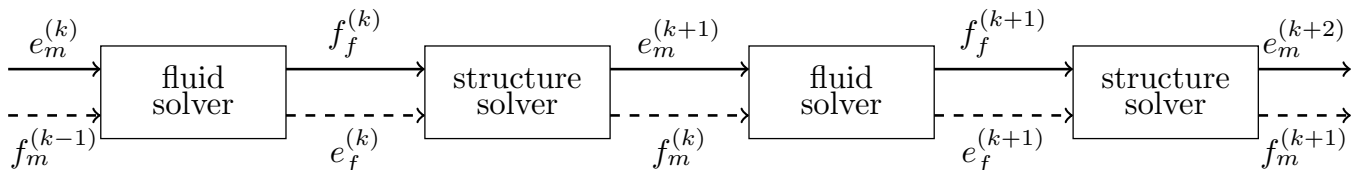


Figure 32: The pressure f_f , and the velocity e_m , are the variables used to update the port-Hamiltonian FSI model, shown by thick arrows; their respective counterparts are shown by dashed arrows.

If we look at only the first *structure solver* component, we can see that we have four variables that are used in this set of equations; $f_f^{(k)}$, $e_f^{(k)}$, $e_m^{(k+1)}$, and $f_m^{(k)}$. It is useful to treat the *exact* equations

$$\begin{aligned} f_m^{(k)} &= -\mathbf{A}f_f^{(k)}, \\ e_f^{(k)} &= \mathbf{A}^T e_m^{(k)}, \end{aligned} \tag{92}$$

as a set of boundary conditions on the solvers, with the first being imposed on the structure solver, and the second being imposed on the fluid solver³¹. More generally, we want these boundary conditions to exist for all iterations – also referred to here as *counts* – so that we can rewrite the equations as

$$\begin{aligned} f_m^{(k)} &= -\mathbf{A}f_f^{(k)}, \\ e_f^{(j)} &= \mathbf{A}^T e_m^{(j)}, \end{aligned} \tag{93}$$

where k and j are counts that are not necessarily equal. As we wish to treat the coupling as a *global* boundary condition, we only require that the counts need to be *pairwise* identical, otherwise we would not have any governing equations which allow for iterative updating.

With this in mind, the structure solver can be thought of such that $f_m^{(k)}$ can be computed directly from the imposed boundary condition, while $e_m^{(k+1)}$ is computed with a numerical error, from the previous count variable, $e_f^{(k)}$. Therefore, we can represent this by the following scheme:

$$\begin{aligned} \text{Structure Solver B.C. : } f_m^{(k)} &= -\mathbf{A}f_f^{(k)}, \\ \text{Balance Equation : } e_f^{(k)} &= \mathbf{A}^T e_m^{(k+1)} + \psi^{(k+1)}, \end{aligned} \tag{94}$$

where $\psi^{(k+1)}$ represents the imbalance between the updated *efforts* over the structure solver.

³¹Note that this does *not* create an exact solver at any point, as for each solver *one* of the variables has a different iteration superscript. It may be useful for the reader to think of this coupling as representing a Dirac structure that cannot be attained within the numerical model, due to the inherent inaccuracies.

A similar approach can then be used to describe the fluid solver, such that we impose the second boundary condition equation, and also find an imbalance between the updated *flows* from one iteration to the next. Thus, we find the new equations

$$\begin{aligned} \text{Balance Equation : } \quad f_m^{(k)} &= -\mathbf{A}f_f^{(k+1)} + \gamma^{(k+1)}, \\ \text{Fluid Solver B.C. : } \quad e_f^{(k+1)} &= \mathbf{A}^T e_m^{(k+1)}, \end{aligned} \tag{95}$$

where we now represent the flow imbalance by the term $\gamma^{(k+1)}$. Note that in neither set of equations do we try to separate $e_m^{(k+1)}$, nor $f_f^{(k+1)}$; indeed, we have not specified that \mathbf{A} is a square matrix, let alone invertible, so we use this formulation to keep everything well-defined.

We can focus on this particular section of the coupling scheme, to give a clearer representation of where the imbalance in the solvers comes from, shown by Fig. 33.

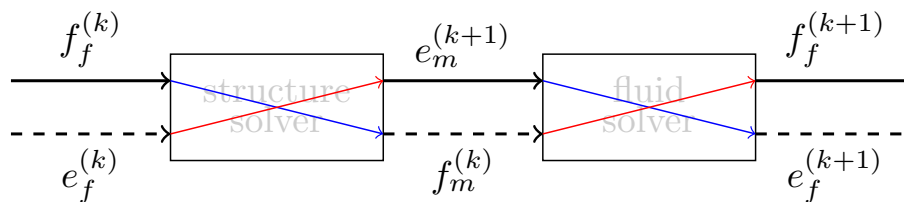


Figure 33: One full cycle, updating the port $(f_f^{(k)}, e_f^{(k)})$ by one count, to $(f_f^{(k+1)}, e_f^{(k+1)})$. Blue arrows denote the *exact* boundary conditions for each solver, while red arrows denote the *inexact* updating of efforts and flows.

Readers may be wondering why we chose to have an apparent offset of one iteration in Figs. 32 and 33, i.e., why the fluid variables have an equal count value, but the mote variables do not. This comes from the fact that we use the exact equations (92) as boundary conditions for the solvers; if we had that all variable pairs had an equal count, then this would mean that one of the solvers was *exact* – whereby all four variables would have the same iteration number (Fig. 34) – and so all of the numerical error would enter through the other solver.

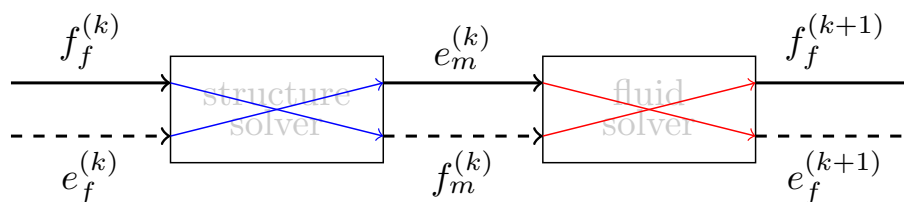


Figure 34: Without the iteration offset, one of the solvers satisfies the boundary condition equations *exactly*, meaning that the other solver must induce *all* of the error in the computations.

This is obviously not the case, therefore we employ a boundary condition for *each* solver, meaning that there is a graphical offset of the iteration number, to represent the fact that we do not have an exact four-tuple of variables at any point in the iterative scheme. The numerical imbalance then comes from the fact that at each iteration, only two of the following three conditions hold:

- the exact coupling equations,
- the exact fluid equations,

- the exact solid equations.

In the general depiction shown by Fig. 31, we noted that in one complete cycle we would update the balance variables *twice*; to amend this slightly, Eqs. (94) and (95) show that in each direction, we only need to update *part* of the balance variables, dependent on which solver is being used. For clarity, we will re-imagine Fig. 31 using two different balance elements – one maintaining the balance over the structure solver, and the other maintaining the balance over the fluid solver – shown by Fig. 35.

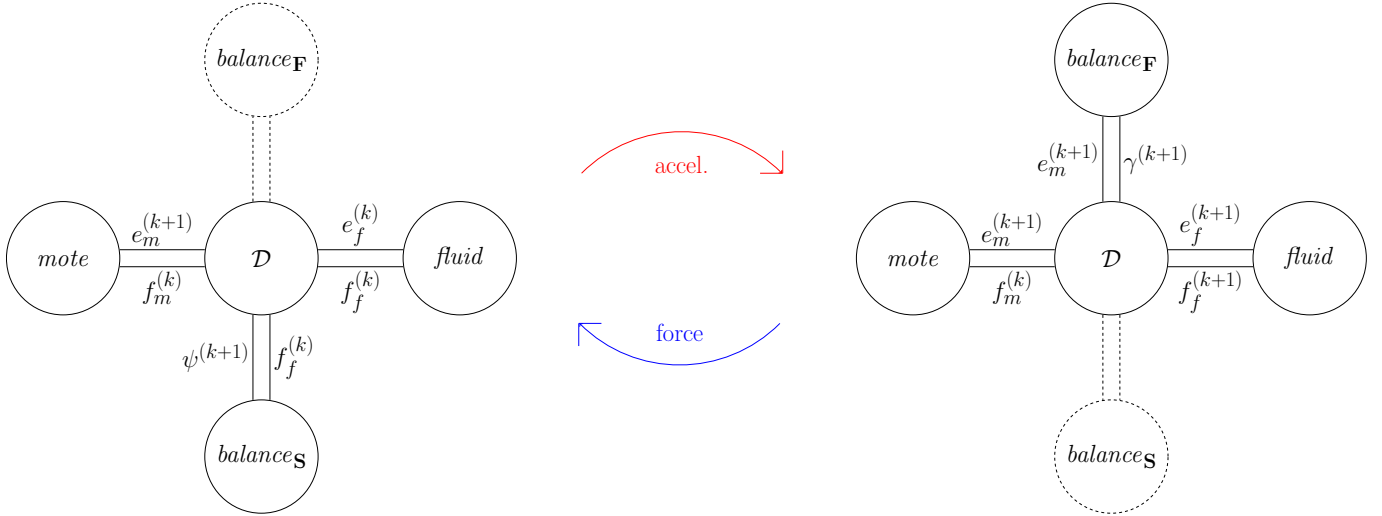


Figure 35: The port-based representation of Fig. 32. Note that the balance element is divided into two, with each part being used *only* with its respective solver (denoted by the subscript). The dashed lines do not mean that the unused balance port is removed from the system, but instead it just has no effect at that given moment, i.e., the effort and flow are equal to zero.

It should hopefully be clear to the reader that the balance elements can still be treated as a whole; we only partition them in this representation to stress which variables are required to maintain the power balance at each iteration. If we wanted, we could have kept the original balance port notation, such that for the structure solver we would have

$$-f_b^{\mathbf{S}} = \begin{bmatrix} \mathbf{0} \\ \cdots \\ \psi^{(k+1)} \end{bmatrix}, \quad \text{and} \quad e_b^{\mathbf{S}} = \begin{bmatrix} \mathbf{0} \\ \cdots \\ f_f^{(k)} \end{bmatrix}, \quad (96)$$

while for the fluid solver we instead would use

$$-f_b^{\mathbf{F}} = \begin{bmatrix} \gamma^{(k+1)} \\ \cdots \\ \mathbf{0} \end{bmatrix}, \quad \text{and} \quad e_b^{\mathbf{F}} = \begin{bmatrix} e_m^{(k+1)} \\ \cdots \\ \mathbf{0} \end{bmatrix}. \quad (97)$$

Given that we want the numerical coupling scheme to converge to accurate, yet approximate, solutions, we necessarily require that the balance terms in *both* solvers tend to zero; indeed, we would not find solutions if only one of the solvers was convergent. Also, we want convergence to occur no matter what state the system is in, i.e., regardless of the efforts and flows of the physical domains. This means that the convergence of the balance product, $e_b^T f_b$, to zero is governed entirely by the error terms, γ and ψ , as mentioned previously. We can therefore represent the numerical error inherent in one full cycle by combining these balance variables such that we define

$$-f_b^{(k+1)} = \begin{bmatrix} \gamma^{(k+1)} \\ \dots \\ \psi^{(k+1)} \end{bmatrix}, \quad \text{and} \quad e_b^{(k+1)} = \begin{bmatrix} e_m^{(k+1)} \\ \dots \\ f_f^{(k)} \end{bmatrix}. \quad (98)$$

Thus, for the balance product to tend to zero regardless of the state of the system, meaning that the numerical scheme tends to the idealised model, we require that the *balance flow* itself tends to zero, i.e.,

$$-f_b^{(k+1)} = \begin{bmatrix} \gamma^{(k+1)} \\ \dots \\ \psi^{(k+1)} \end{bmatrix} \rightarrow \begin{bmatrix} 0 \\ 0 \\ \vdots \\ 0 \\ 0 \end{bmatrix} \quad \text{as } k \rightarrow \infty. \quad (99)$$

In modelling terms, we would not necessarily need the balance flow to actually reach zero, as we would have a predetermined tolerance that would be specified within the simulation. Therefore, as soon as the additional power $e_b^T f_b$ was less than the prescribed tolerance, then the next time step would be initialised. Even more specifically, due to the fact that we are working in the field \mathbb{F} there would not necessarily be a smooth convergence to zero, as we would eventually fall below machine precision values, and so the discretized model would have an energy balance, yet it would only be a machine-accurate approximation of the idealised port-Hamiltonian model.

The depiction given by Fig. 35, and the balance port criterion (99) represent the first attempt in bridging the gap between computational modelling, and port-Hamiltonian systems. It may be possible to use ideas from Lequeurre and Tucsnaak [13] or Talasila et al. [26] to extend upon this basic foundation, but for now this tentative step should hopefully suffice.

8 Discussion

In this project, we analysed the applicability of CFD software such as *ComFLOW* to the problem of modelling WiseMotesTM within pipelines, with an importance placed on the effects of initial position, and relative size of the mote. We also used the simulations to confirm the efficiency of the *quasi-simultaneous* coupling method, finding that the computational load was heavily decreased for nearly all simulations, agreeing with the work by Veldman et al. [35, 36]. The trajectory results that were obtained also seemed to agree with initial results from INCAS³ experimentation, suggesting that more detailed simulations can, and should, be constructed.

The progression into a port-Hamiltonian framework was not as smooth as initially expected, and indeed a lot of time was spent following avenues that turned out to not be entirely useful for this project. Problems were encountered in the rigorous formulation of the Hamiltonian equations, but general ideas were explored, after assuming that a useful Hamiltonian *did* exist. The extension of the coupled iteration schemes also found a general form, using the lattice \mathbb{F}^n , rather than an abstract vector space. The lack of available literature was a major hurdle for this part of the project, forcing research to extend in directions that were *far* beyond the level of a Bachelor's thesis. However, hopefully there are enough ideas included in this study, that further exploration has a foundation to build upon.

Regarding the question presented by INCAS³, it is now apparent that this is a *very* deep topic, and the construction of computational models may need to go hand-in-hand with further experimentation, especially to verify the effects of motes with relatively large radii. However, the initial results shown here present a very basic understanding of the problem, which again may be useful for future work.

8.1 Possible extensions

With respect to the simulations of this project, there are two areas of extension which would probably be of the most use at this point in time. Firstly, it could prove useful if future work focused on trying to mirror any experimental data that has already been captured by INCAS³. This would allow a two-way confirmation of results, such that the accuracy of simulations could be verified by their approximation to actual experiments, but also the flow behaviour of such experiments may be able to be analysed in a much more detailed way, e.g., using graphical pressure fields to understand the forces acting at each moment in time.

A second possible direction would be to cross-examine the effects of altering the mote size *and* the initial position, to observe what effect these combined changes have on the trajectory plots. This would be interesting if it were found that there was an observable Segré-Silberberg effect acting on the motes, causing them to have a non-central equilibrium position. However, an investigation such as this may also be better served if there were available experimental data for different pipe widths, such that the simulations could also be verified to be approximating *actual* flow behaviour correctly.

Alternatively, it may be useful to model less simple models, such that tentative steps can be made into the field of rebuilding pipe geometries from captured acceleration and rotation data. Already, some very basic examples have been made by the Computational Mechanics and Numerical Mathematics department, of uniform pipelines with small, wall indentations, showing the general effect on the mote rotation and acceleration values. Again, this may be more beneficial alongside compara-

tive studies by INCAS³, so that general behaviour could be verified for the simple cases, from which larger, more complex models can be built.

Regarding the development of a port-Hamiltonian model, there will need to be a lot more work invested in understanding how to represent a multi-dimensional fluid model in the necessary language. Although we hoped that the article by Lequeurre and Tucsnak [13] would be a useful starting point for this study, the jump from a one-dimensional model with only two geometric and kinematic constraints to even a two-dimensional model is not an easy task to undertake. Once more robust theory has been developed for this type of representation, it will then prove useful to analyse the previous approach using this new foundation, as we would not have to rest so many assumptions on the inclusion of an unknown Hamiltonian function. Also, the necessary surface coupling *function* would hopefully become more clear, possibly mirroring the ideas taken from Hamiltonian fluid mechanics, discussed in Sections 6.2.1 and 6.2.2.

Alternatively, it could instead be of use to describe both the solid *and* fluid domain in terms of mechanical domains, meaning that the coupling conditions may even become more intuitive. This direction was explored only slightly, as an afterthought to all previous work, and was not felt to add anything of value to this the current work. However, this approach could perhaps solve some of the coupling difficulties, as the domain variables will all be of the same form.

Once these foundations are understood more concretely, a stricter formulation of coupling schemes can be attempted, to be built on a more well-defined base. It would certainly be both interesting and rewarding to present the quasi-simultaneous coupling method in terms of combinations of flows and efforts, to view the entire scheme as an iterative port-Hamiltonian system. In addition to this, in Section 9.6 we have included a brief look into the realm of *co-simulation*, which could also be a rich area of investigation, as concepts may be able to be borrowed which could be more representative of the behaviour we are trying to describe.

With all of these possible directions, we hope that this study will be of some merit for future research.

9 Appendices

9.1 Table of geometric models

The following table is a reference for all simulation sets that were completed for this thesis.

Method	Focus	No. of Sims.	Geometry	Grid Size	Comments
Weak	Mote Radius	25	$[-2, 4] \times [-0.3, 0.3]$	120×12	
	Mote Radius	9	$[-2, 4] \times [-0.3, 0.3]$	240×24	
	Mote Radius	25	$[-2, 4] \times [-0.3, 0.3]$	120×12	Neutral density
	Mote Radius	9	$[-2, 4] \times [-0.3, 0.3]$	240×24	Neutral density
	x-Position	11	$[-2, 2] \times [-0.3, 0.3]$	80×12	Neutral density
	y-Position	25	$[-2, 4] \times [-0.3, 0.3]$	120×12	
Quasi	Mote Radius	25	$[-2, 4] \times [-0.3, 0.3]$	120×12	
	Mote Radius	9	$[-2, 4] \times [-0.3, 0.3]$	240×24	
	Mote Radius	25	$[-2, 4] \times [-0.3, 0.3]$	120×12	Neutral density
	Mote Radius	9	$[-2, 4] \times [-0.3, 0.3]$	240×24	Neutral density
	x-Position	11	$[-2, 2] \times [-0.3, 0.3]$	80×12	Neutral density
	y-Position	25	$[-2, 4] \times [-0.3, 0.3]$	120×12	
	y-Position	9	$[-2, 6] \times [-0.3, 0.3]$	160×12	15 seconds
	y-Position	9	$[-2, 6] \times [-0.3, 0.3]$	320×24	15 seconds
	y-Position	8	$[-2, 6] \times [-0.3, 0.3]$	320×24	Revised code

In addition to this, around 100 simulations were completed at the beginning of this project, but it was discovered that the effect of shear forces was not implemented in any of the models. For this reason, all data from simulations before this point was *not* included in this thesis, as it was seen to be non-representative of the actual physical behaviour.

9.2 Additional results

The following plots show the total pressure solves and added mass ratios, when using the neutrally dense mote over the finer grid. The results are not as clear-cut as Figs. 16 and 17, due to the smaller number of simulations. However, the behaviour is still the same, with an increase in radius creating an increase in both the added mass and the number of pressure solves needed.

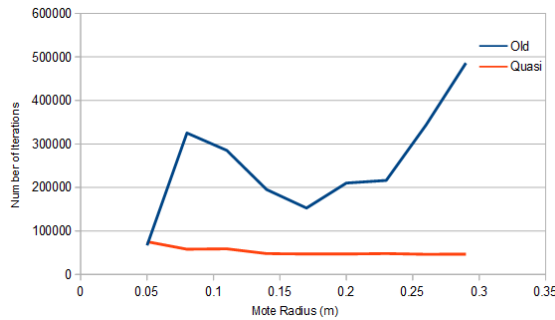


Figure 36: Total Number of pressure solves, using a neutrally dense mote. Grid: 240×24 .

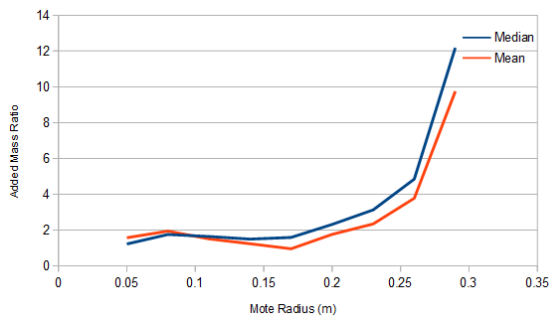


Figure 37: Median and mean added mass ratios, using a neutrally dense mote. Grid: 240×24 .

The reason for the unexpected similarity between the two methods at the left side of Fig. 36 is due to the fact that *ComFLOW* could not complete the full simulation using the weakly coupled method,

so the first value is *not* representative of the total number of pressure solves.

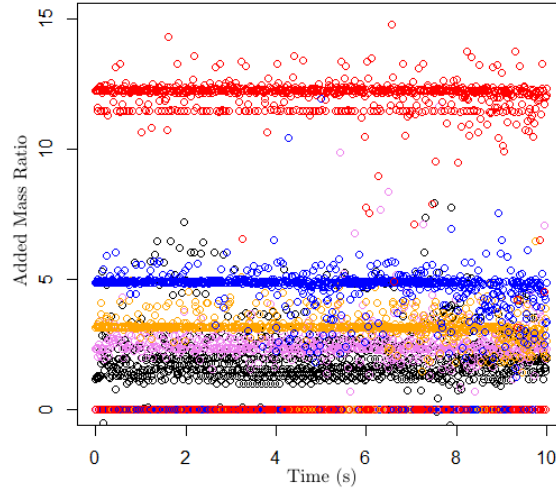


Figure 38: Plot of the distributed added mass ratios for multiple data sets, over the fine grid.

Fig. 38 shows the distributed mass ratios over the finer grid, using the same radial values as Fig. 18, and again the behaviour agrees with the coarse grid. The distribution is slightly more scattered, which could be due to the increase in grid points, and therefore a more mixed distribution. However, there are still clear levels which distinguish the different radius sizes, showing that there is a direct impact of mote size on the added mass ratio.

9.3 Table of domain classifications

This table shows the various storage elements, flows, and efforts for different port-Hamiltonian domains.

physical subdomain	flow $f \in \mathcal{F}$	effort $e \in \mathcal{E}$	storage state $x \in \mathcal{X}$
electric	current	voltage	charge
magnetic	voltage	current	flux linkage
potential translation	velocity	force	displacement
kinetic translation	force	velocity	momentum
potential rotation	angular velocity	torque	angular displacement
kinetic rotation	torque	angular velocity	angular momentum
potential hydraulic	volume flow	pressure	volume
kinetic hydraulic	pressure	volume flow	flow tube momentum
chemical	molar flow	chemical potential	number of moles
thermal	entropy flow	temperature	entropy

9.4 Canonical Hamiltonian form

We present here a reduced derivation for the *canonical* Hamiltonian description of fluid dynamics, taken from a paper by Philip Morrison [16]. If at any point the reader is not sure of something, we advise them to consult the original text for clarification.

In this derivation we will be looking at the Lagrangian formulation of a fluid domain D , such that the position of each fluid element is specified by the variable $q = q(a, t)$, where $q = (q_1, q_2, q_3)^T$ and $a = (a_1, a_2, a_3)^T$. Here we treat a as an identifying label given to each fluid particle at $t = 0$, such that we can ‘track’ its position over time. Without going into any thermodynamics, we will look at the potential energy of a fluid as a function of pressure and temperature, and so we will use the energy per unit mass, U , as a function of mass density, ρ , and entropy per unit mass, s . However, these are Eulerian variables, and so they must be described in terms of Lagrangian variables.

To remind the reader, an Eulerian view of a fluid looks at a single point in the domain and watches how the properties at that particular point change through time, i.e., flow velocity, density, etc. Conversely, a Lagrangian viewpoint takes a specific fluid element and follow its path throughout the domain, keeping track of how its own *specific* variables change over time.

If we take r as the Eulerian *spatial* variable, such that it describes a position in the domain, then the Eulerian density is given by

$$\rho(r, t) = \int_D \delta(r - q(a, t)) \rho_0(a) d^3 a, \quad (100)$$

where $\rho_0(a)$ is the (pointwise) initial mass density of each fluid particle, and $\delta(r - q)$ is a three-dimensional Dirac delta function. This can instead be written as

$$\rho(r, t) = \left. \frac{\rho_0(a)}{\mathcal{J}(a, t)} \right|_{a=q^{-1}(r, t)} \quad (101)$$

where $\mathcal{J} = \det(\partial q_i / \partial a_j)$, which when combined with $\rho d^3 q = \rho_0 d^3 a$, and $d^3 q = \mathcal{J} d^3 a$ finds a representation of mass conservation.

Similar to Eq. (100), we can also find forms for the *entropy per unit volume*,

$$\sigma(r, t) = \int_D \sigma_0(a) \delta(r - q(a, t)) d^3 a, \quad (102)$$

with $\sigma_0(a) = r h_0(a) s_0(a)$, and the momentum density,

$$M(r, t) = \int_D \dot{q}(a, t) \delta(r - q(a, t)) \rho_0(a) d^3 a. \quad (103)$$

Therefore, the counterparts of Eq. (101) are

$$\begin{aligned} s(r, t) &= \left. s_0(a) \right|_{a=q^{-1}(r, t)} \\ v(r, t) &= \left. \dot{q}(a, t) \right|_{a=q^{-1}(r, t)} \end{aligned} \quad (104)$$

where the second equation is the relation between Eulerian and Lagrangian velocities.

Now if we take the energy per unit volume, ρU , then the total potential energy of the fluid is given by

$$V [q] = \int_D \rho_0 U(s_0, \rho_0 / \mathcal{J}) d^3 a. \quad (105)$$

In addition, the kinetic energy is simply given by

$$T[\dot{q}] = \frac{1}{2} \int_D \rho_0 \dot{q}^2 d^3 a. \quad (106)$$

Therefore, the *Lagrangian* itself is defined as

$$\begin{aligned} L[q, \dot{q}] &= T[\dot{q}] - V[q], \\ &= \int_D \left(\frac{1}{2} \rho_0 \dot{q}^2 - \rho_0 U \right) d^3 a, \\ &=: \int_D \mathcal{L}(q, \dot{q}, \frac{\partial q}{\partial a}, t) d^3 a, \end{aligned} \quad (107)$$

where \mathcal{L} is the *Lagrangian density*. Now we find that the *action* is described by

$$\begin{aligned} S[q] &= \int_{t_0}^{t_1} L[q, \dot{q}] dt, \\ &= \int_{t_0}^{t_1} dt \int_D \left(\frac{1}{2} \rho_0 \dot{q}^2 - \rho_0 U \right) d^3 a, \end{aligned} \quad (108)$$

which has infinitely many degrees of freedom.

We now wish to use *Hamilton's principle* $\delta S / \delta q(a, t) = 0$, which means that we require

$$\frac{d}{dt} \left(\frac{\partial \mathcal{L}}{\partial \dot{q}^i} \right) + \frac{\partial}{\partial a^j} \left(\frac{\partial \mathcal{L}}{\partial q_{,j}^i} \right) - \frac{\partial \mathcal{L}}{\partial q^i} = 0. \quad (109)$$

This condition holds if the surface integral vanishes in Lagrangian coordinates, such that

$$\int_{t_0}^{t_1} \int_{\partial D} p \delta q \cdot \hat{n} d^2 q = 0, \quad (110)$$

which is satisfied with the valid condition of *zero boundary flux*, $\delta q \cdot \hat{n} = 0$.

Using Eq. (109), we find the governing equation,

$$\rho_0 \ddot{q}_i + A_i^j \frac{\partial}{\partial a_j} \left(\frac{\rho_0^2}{\mathcal{J}^2} \frac{\partial U}{\partial \rho} \right) = 0, \quad (111)$$

where we use the shorthand,

$$A_k^i = \frac{1}{2} \epsilon_{kjl} \epsilon_{imn} \frac{\partial q_j}{\partial a_m} \frac{\partial q_l}{\partial a_n}, \quad (112)$$

with ϵ_{ijk} being the skew-symmetric tensor.

Finally, the *Legendre transform* then finds the *canonical momentum density*,

$$\pi_i(a, t) := \frac{\delta L}{\delta \dot{q}_i(a)} = \rho_0 \dot{q}_i \quad (113)$$

and the Hamiltonian,

$$\begin{aligned} H[\pi, q] &= \int \left(\pi \cdot \dot{q} - \mathcal{L} \right) d^3 a, \\ &= \int \left(\frac{\pi^2}{2\rho_0} + \rho_0 U \right) d^3 a, \end{aligned} \quad (114)$$

which are used within this thesis.

9.5 Non-symmetric computations

To appease any skeptical readers, we include here the equations in the main text which follow on from the assumption of using a symmetric relationship, only now we re-write them using the more general form

$$\begin{aligned} f_m &= -\mathbf{A}_1 f_f, \\ e_f &= \mathbf{A}_2 e_m. \end{aligned} \quad (115)$$

The matrix equations (79) now use two separate matrices, such that we have the equations

$$\begin{aligned} f_m &= -\mathbf{A}_1 f_f, \\ e_f &= \mathbf{A}_2 e_m. \end{aligned} \quad (116)$$

This then means that error equations (89) now have the form

$$\begin{aligned} f_m &= -\mathbf{A}_1 f_f + \gamma, \\ e_f &= \mathbf{A}_2 e_m + \psi. \end{aligned} \quad (117)$$

The balance duality product (90) is therefore determined by

$$\begin{aligned} e_b^T f_b &= -\left(e_m^T f_m + e_f^T f_f \right), \\ &= -\left(e_m^T (-\mathbf{A}_1 f_f + \gamma) + (\mathbf{A}_2 e_m + \psi)^T f_f \right), \\ &= e_m^T \mathbf{A}_1 f_f - e_m^T \gamma - e_m^T \mathbf{A}_2^T f_f - \psi^T f_f, \\ &= -(\langle e_m, \gamma \rangle + \langle \psi, f_f \rangle) + e_m^T (\mathbf{A}_1 - \mathbf{A}_2^T) f_f. \end{aligned} \quad (118)$$

The usefulness of assuming $\mathbf{A}_1 = \mathbf{A}_2^T$ is apparent here, as the duality product is more complex than before. However, the additional term should be a scalar, so we can add it to the balance vectors (91) such that

$$-f_b = \begin{bmatrix} \gamma \\ \dots \\ \psi \\ \dots \\ \xi \end{bmatrix}, \quad \text{and} \quad e_b = \begin{bmatrix} e_m \\ \dots \\ f_f \\ \dots \\ 1 \end{bmatrix}, \quad (119)$$

where $\xi = -e_m^T (\mathbf{A}_1 - \mathbf{A}_2^T) f_f$.

The coupling equations (94) and (95) are now rewritten as

$$\text{Structure Solver: } \begin{cases} f_m^{(k)} = -\mathbf{A}_1 f_f^{(k)}, \\ e_f^{(k)} = \mathbf{A}_2 e_m^{(k+1)} + \psi^{(k+1)}, \end{cases} \quad (120)$$

$$\text{Fluid Solver: } \begin{cases} f_m^{(k)} = -\mathbf{A}_1 f_f^{(k+1)} + \gamma^{(k+1)}, \\ e_f^{(k+1)} = \mathbf{A}_2 e_m^{(k+1)}. \end{cases} \quad (121)$$

Finally, this means that for the system to tend to a power balance, (99) is now of the form

$$-f_b^{(k+1)} = \begin{bmatrix} \gamma^{(k+1)} \\ \dots \\ \psi^{(k+1)} \\ \dots \\ \xi^{(k+1)} \end{bmatrix} \rightarrow \begin{bmatrix} 0 \\ 0 \\ \vdots \\ \vdots \\ 0 \\ 0 \end{bmatrix}, \quad \text{as } k \rightarrow \infty. \quad (122)$$

This means that we have the *new* constraint of $\xi^{(k+1)} \rightarrow 0$, i.e., $\{e_m^T(\mathbf{A}_1 - \mathbf{A}_2^T)f_f\}^{(k+1)} \rightarrow 0$. Given that we wish this to hold for general flows and efforts from both domains, this reduces the requirement to $(\mathbf{A}_1 - \mathbf{A}_2^T)^{(k+1)} \rightarrow 0$. This would suggest that even though we did not begin with the symmetric assumption, for the power balance to be conserved we will require that the matrices develop over time such that they *become* symmetric, or at least within a desired accuracy. However, as hinted at in the main text, this adds the problem of having to update the coupling structure with *every* iteration, which is a more difficult task than just updating flows, efforts, and errors.

9.6 Co-simulation: an alternate approach

Given that there is very little literature on Hamiltonian fluids, port-Hamiltonian descriptions of fluids, or port-based fluid FSI models, it has been necessary to expand the reach of this thesis into areas which would otherwise not have been explored. This very brief section draws from a number of articles which focus on *co-simulation*, the coupled simulation of multi-body systems, largely in the field of mechanical engineering. In particular, articles by Kübler and Schiehlen [12], Tomulik and Frączek [28], and Benedikt et al. [3] provide interesting counterparts to areas that we have already explored, such as convergence and stability, and even *algebraic loop* feedback, linking with the added mass criteria of numerical convergence.

The description that follows will be a broad-stroke generalization of what may *possibly* be useful for others to explore, to make stronger links between different disciplines. From Benedikt et al., we borrow a graphical description of a 2 degree-of-freedom oscillator to describe the co-simulation set-up, shown below.

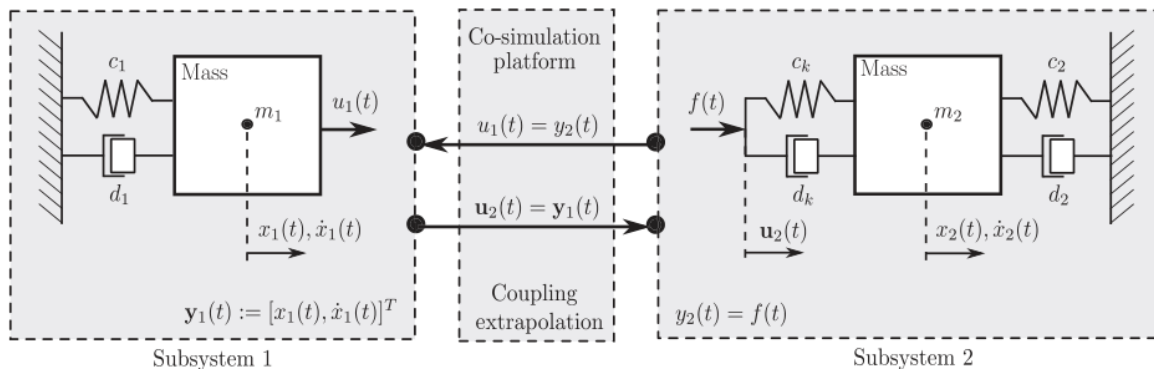


Figure 39: Co-simulation set-up of a coupled 2-DoF oscillator

Using this as a foundation, we present a similar graphical description of the quasi-simultaneous coupling method, shown by Fig. 40.

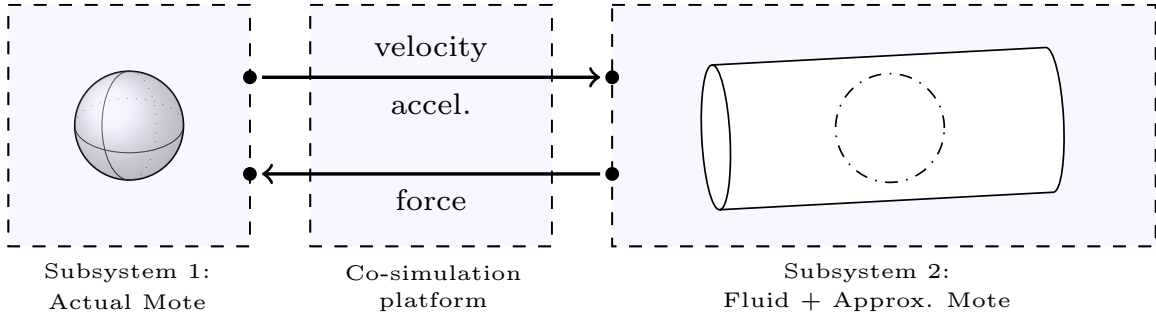


Figure 40: Co-simulation set-up of the fluid-structure interaction system, governed by the quasi-simultaneous method.

Clearly, the FSI system cannot be represented in the same way as the oscillator, due to the infinite degrees-of-freedom of the fluid. However, we still have a direction of forces and motions, in the same way that Fig. 7 has directions of forces and accelerations, which is the exact coupling method that we are trying to describe.

The main difference with this description is that rather than treat the mote and the fluid as an ideal subsystem, with the balance element being the disturbance, we instead treat the fluid and *approximate mote* as the ideal system, with the *actual mote* acting as the ‘disturbance’. The reasoning for this is quite simple – in the quasi-simultaneous method the fluid ‘anticipates’ the response of the mote, so the energy balance between the fluid and the *approximate mote* is maintained. Thus, when the *actual mote* subsystem is added, it is highly likely that the approximate and actual motes will not be identical, and so we have the ‘disturbance’. It is important to see that although Subsystem 2 *is* maintained by a Dirac structure, the coupling of the two subsystems is not, due to the difference in the two motes.

Keeping this in mind, via the intuition of Prof. Veldman we present a new graphical representation of the quasi-simultaneous method, given in terms of ‘*pseudo-port-Hamiltonian*’ notation, shown by Fig. 41.

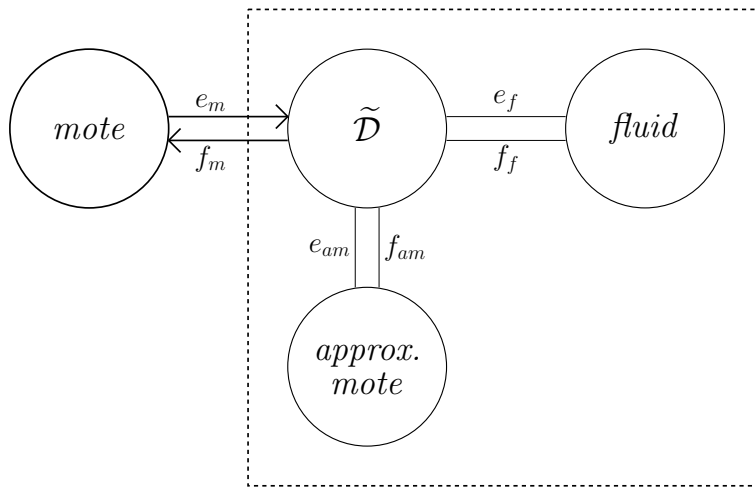


Figure 41: A ‘pseudo-port-Hamiltonian’ representation of the quasi-simultaneous coupling method.

Here we keep the notation of flows and efforts, in an attempt to maintain the link with port-Hamiltonian systems, but we include the new notation of directed arrows and a dashed-box partition. The dashed-box graphically represents that the system *within* is governed by a Dirac structure, $\tilde{\mathcal{D}}$, while the addition of *outside* elements destroys this property. As well as this, the box also represents the *co-simulation platform* over which we must exchange information. Also, rather than have undirected port bonds, we include directed arrows between the ‘Dirac’ and ‘non-Dirac’ components, to show the direction of the iterative coupling, i.e., the flow (force) impacts upon mote, which then outputs an effort (velocity) to affect the fluid *and* approximate mote.

It would be nice to be able to represent this quasi-simultaneous system in an equation form, similar to Eqs. (94) and (95). However, due to the approximate mote, we would likely need to use a combination of flows and efforts to describe the inputs and outputs of each subsystem, which is not necessarily an easy task. Therefore, it falls beyond the remit of this study, but the idea has been planted for any future work. Although this brief description of the quasi-simultaneous coupling method is given in a very loose manner, we felt it was interesting to summarise the attempted collaboration between computation mathematics and port-Hamiltonian systems, bringing together all previous discussion into a single graphical description.

References

- [1] J. D. Anderson Jr. *Computational fluid dynamics: the basics with applications*. McGraw-Hill series in aeronautical and aerospace engineering. McGraw-Hill Inc., 1995.
- [2] I. Antoniou and G.P. Pronko. On the hamiltonian description of fluid mechanics. *arXiv preprint hep-th/0106119*, 2001.
- [3] M. Benedikt, D. Watzenig, and A. Hofer. Modelling and analysis of the non-iterative coupling process for co-simulation. *Mathematical and Computer Modelling of Dynamical Systems*, 19(5):451–470, 2013.
- [4] C.E. Brennen. A review of added mass and fluid inertial forces. 1982.
- [5] P. Causin, J.F. Gerbeau, and F. Nobile. Added-mass effect in the design of partitioned algorithms for fluid–structure problems. *Computer methods in applied mechanics and engineering*, 194(42):4506–4527, 2005.
- [6] R.G. Cox and H. Brenner. The lateral migration of solid particles in poiseuille flow — i: Theory. *Chemical Engineering Science*, 23(2):147–173, 1968.
- [7] B.P. Epps and A.H. Techet. *2.016 hydrodynamics: derivation of added mass around a sphere*.
- [8] S. Fackrell. Study of the added mass of cylinders and spheres. 2011.
- [9] J. Feng, H.H. Hu, and D.D. Joseph. Direct simulation of initial value problems for the motion of solid bodies in a newtonian fluid. part 2: couette and poiseuille flows. *Journal of fluid mechanics*, 277:271–301, 1994.
- [10] A. Hogg. The inertial migration of non-neutrally buoyant spherical particles in two-dimensional shear flows. *Journal of Fluid Mechanics*, 272:285–318, 1994.
- [11] A. Karnis, H.L. Goldsmith, and S.G. Mason. The flow of suspensions through tubes: V. inertial effects. *The Canadian Journal of Chemical Engineering*, 44(4):181–193, 1966.
- [12] R. Kübler and W. Schiehlen. Modular simulation in multibody system dynamics. *Multibody System Dynamics*, 4(2-3):107–127, 2000.
- [13] J. Lequeurre and M. Tucsnaak. The piston problem in a port-hamiltonian formalism. *IFAC-PapersOnLine*, 48(13):212–216, 2015.
- [14] X. Liang. *Numerical study of flow around bypass pigs*. PhD thesis, Delft University of Technology, 2015.
- [15] D. Morin. *Introduction to classical mechanics: with problems and solutions*. Cambridge University Press, 2008.
- [16] P.J. Morrison. Hamiltonian description of the ideal fluid. *Reviews of modern physics*, 70(2):467, 1998.
- [17] P.J. Morrison. Hamiltonian fluid dynamics. *Encyclopedia of mathematical physics*, 2, 2006.
- [18] J. Pantaleone and J. Messer. The added mass of a spherical projectile. *American Journal of Physics*, 79(12):1202–1210, 2011.
- [19] H.M. Paynter. *Analysis and design of engineering systems*. Cambridge, MA: MIT Press, 1961.
- [20] J. Poiseuille. *Observations of blood flow*. *Ann. Sci. Nat.*, 5(2), 1836.

- [21] A. Quarteroni, F. Saleri, and Gervasio P. *Scientific computing with MATLAB and Octave*. Texts in computational science and engineering. Springer Berlin Heidelberg, 4th edition, 2014.
- [22] R. Salmon. Hamiltonian fluid mechanics. *Annual review of fluid mechanics*, 20(1):225–256, 1988.
- [23] J.A. Schonberg and E.J. Hinch. Inertial migration of a sphere in poiseuille flow. *Journal of Fluid Mechanics*, 203:517–524, 1989.
- [24] G. Segré and A. Silberberg. Behaviour of macroscopic rigid spheres in poiseuille flow. part 1. determination of local concentration by statistical analysis of particle passages through crossed light beams. *Journal of Fluid Mechanics*, 14(1):115–135, 1962.
- [25] G. Segré and A. Silberberg. Behaviour of macroscopic rigid spheres in poiseuille flow. part 2. experimental results and interpretation. *Journal of Fluid Mechanics*, 14(1):136–157, 1962.
- [26] V. Talasila, J. Clemente-Gallardo, and A.J. van der Schaft. Discrete port-hamiltonian systems. *Systems & control letters*, 55(6):478–486, 2006.
- [27] A.H. Techet. *2.016 hydrodynamics: added mass*.
- [28] P. Tomulik and J. Frączek. Simulation of multibody systems with the use of coupling techniques: a case study. *Multibody System Dynamics*, 25(2):145–165, 2011.
- [29] A.J. van der Schaft. Port-hamiltonian systems: an introductory survey. 2006.
- [30] A.J. van der Schaft and J. Cervera. Composition of dirac structures and control of port-hamiltonian systems. 2002.
- [31] A.J. van der Schaft and D. Jeltsema. Port-hamiltonian systems theory: an introductory overview. *Foundations and Trends in Systems and Control*, 1(2-3):173–378, 2014.
- [32] W. van Saarloos, D. Bedeaux, and P. Mazur. Hydrodynamics for an ideal fluid: hamiltonian formalism and liouville-equation. *Physica A: Statistical Mechanics and its Applications*, 107(1):109–125, 1981.
- [33] A.E.P. Veldman. New, quasi-simultaneous method to calculate interacting boundary layers. *AIAA journal*, 19(1):79–85, 1981.
- [34] A.E.P. Veldman. *Computational fluid dynamics - lecture notes in applied mathematics*, 2012.
- [35] A.E.P. Veldman, R. Luppés, P. van der Plas, H. van der Heiden, B. Düz, H. Seubers, J. Helder, T. Bunnik, and R. Huijsmans. *Free-surface flow simulations for moored and floating offshore platforms*. VII European Congress on Computational Methods in Applied Sciences and Engineering - Crete, Greece, 5–10 June 2016.
- [36] A.E.P. Veldman, R. Luppés, P. van der Plas, H. van der Heiden, H. Seubers, B. Düz, R. Huijsmans, J. Helder, and T. Bunnik. *Locally-refined free-surface flow simulations for moored and floating offshore platforms*.
- [37] D. Wirosoetisno. *Lagrangian and hamiltonian methods in geophysical fluid dynamics*. Citeseer.
- [38] B.H. Yang, J. Wang, D.D. Joseph, H.H. Hu, T.W. Pan, and R. Glowinski. Migration of a sphere in tube flow. *Journal of Fluid Mechanics*, 540:109–131, 2005.
- [39] B.H. Yang, J. Wang, D.D. Joseph, H.H. Hu, T.W. Pan, and R. Glowinski. Numerical study of particle migration in tube and plane poiseuille flows. In *IUTAM Symposium on Computational Approaches to Multiphase Flow*, pages 225–235. Springer, 2006.

Works not directly referenced

The following texts were looked at during this study, but were not directly referred to within the body of the thesis.

[i] N.J. Balmforth, and P.J. Morrison. Hamiltonian description of shear flow. *Large-Scale Atmosphere-Ocean Dynamics II*, 117–142, 2002.

[ii] V. Duindam, A. Macchelli, S. Stramigioli, and H. Bruyninckx. *Modeling and control of complex physical systems: the port-Hamiltonian approach*. Springer Science & Business Media, 2009.

[iii] K.D. Klotsa. *The dynamics of spheres in oscillatory fluid flows*. PhD Thesis, University of Nottingham, 2009.

[iv] J.H. Maddocks, and R.L. Pego. An unconstrained hamiltonian formulation for incompressible fluid flow. *Communications in mathematical physics*, 170:107–217, 1995.

[v] A.E.P. Veldman. *Viscous-inviscid interaction, partitioned dynamical systems and i(n)te(g)ration*, TP 89232 L. NLR - Netherlands Aerospace Centre, 1989.

[vi] H.H. Yi. The lift force on a spherical particle in rectangular pipe flow. *Chinese Journal of Physics*, 52:174–184, 2014.

[vii] H. Zhang, H. Mao, and G. Peng. Modular collaborative simulation in multibody system dynamics of complex mechatronic products. *2013 IEEE International Conference on Systems, Man, and Cybernetics*, 705–711, 2013.

[viii] *Notes for C5.7: Topics in Fluids*. University of Oxford, 2015.

[ix] *Part A: Fluid Dynamics and Waves*. University of Oxford, 2014.